

# Hot Degenerate Components in Blue Stragglers: A Multi-Wavelength SED Analysis of Nine Open Clusters with Swift/UVOT

DENİZ CENNET ÇINAR <sup>1</sup>, D. BISHT <sup>2</sup>, SELÇUK BILIR <sup>3</sup>, SONGMEI QIN <sup>4,5,6</sup> AND LEILA SAKER <sup>7</sup>

<sup>1</sup>*Istanbul University, Institute of Graduate Studies in Science, Programme of Astronomy and Space Sciences, 34116, Istanbul, Turkey*  
<sup>2</sup>*Indian Centre for Space Physics, 466, Barakhola, Singabari Road, Netai Nagar, Kolkata, West Bengal, 700099, India*  
<sup>3</sup>*Istanbul University, Faculty of Science, Department of Astronomy and Space Sciences, 34119, Beyazıt, Istanbul, Turkey*  
<sup>4</sup>*Astrophysics Division, Shanghai Astronomical Observatory, Chinese Academy of Sciences, Shanghai 200030, China*  
<sup>5</sup>*School of Astronomy and Space Science, University of Chinese Academy of Sciences, No. 19A, Yuquan Road, Beijing 100049, PR China*  
<sup>6</sup>*Institut de Ciències del Cosmos (ICCUB), Universitat de Barcelona (UB), Martí i Franquès 1, E-08028 Barcelona, Spain*  
<sup>7</sup>*Observatorio Astronómico, Universidad Nacional de Córdoba, Laprida 854, 5000 Córdoba, Argentina*

## ABSTRACT

We present a homogeneous multi-wavelength analysis of 35 blue straggler star (BSS) candidates in nine open clusters, combining *Swift*/UVOT near-ultraviolet data with Gaia DR3 astrometry and optical-to-infrared photometry. We construct spectral energy distributions (SEDs) to search for signatures of hot companions associated with past mass transfer. Among the sample, 15 BSSs ( $\sim 43\%$ ) show ultraviolet excesses that are better described by two-component SED fits. The inferred companions are consistent with hot white dwarfs and pre-extremely low-mass (pre-ELM) white dwarf candidates, suggesting systems observed at different stages following mass transfer. We examine the radial distribution of the BSSs and find evidence for mass segregation in dynamically evolved clusters, a result that is broadly consistent with the estimated half-mass relaxation timescales of the host systems. To place the clusters in a Galactic context, we compute their orbits using *galpy*, obtaining low eccentricities ( $e \leq 0.1$ ) and disk-like trajectories. We also find a positive relation between the half-number radius of the BSS population ( $r_{50}$ ) and the total number of BSSs. Overall, our results are consistent with a scenario in which the BSS population in these clusters is dominated by binary evolution. The systems identified here provide observational constraints on post-mass-transfer evolutionary phases. While the number of robust detections is limited and intrinsic degeneracies remain in SED-based decomposition, these results provide a useful foundation for future spectroscopic confirmation.

**Keywords:** Blue straggler stars (168); Open star clusters (1160); Stellar evolution (1599), Ultraviolet astronomy (1736)

## 1. INTRODUCTION

Blue straggler stars (BSSs), first identified by Sandage (1953), are stars in stellar clusters that appear anomalously brighter and hotter than the main-sequence turn-off (MSTO), suggesting rejuvenation relative to the dominant cluster population. Their position in color-magnitude diagrams (CMDs) cannot be explained by standard single-star evolution at the cluster age, making BSSs valuable laboratories for investigating non-standard evolutionary pathways, particularly those in-

volving binary interactions and stellar dynamics (e.g., Baily 1995; Ferraro et al. 2009).

Two principal formation channels are commonly invoked to explain the origin of BSSs. The first involves mass transfer or common-envelope evolution in binary systems, in which a star accretes mass from an evolved companion (McCrea 1964). The second channel involves stellar collisions or mergers between low-mass stars (Hills & Day 1976). While collisional processes are expected to contribute significantly in the dense environments of globular clusters (GCs), numerous observational and theoretical studies indicate that mass transfer is the dominant mechanism in the relatively sparse environments of open clusters (OCs) (Knigge et al. 2009; Mathieu & Geller 2009).

**Table 1.** Literature survey of BSSs in OCs.

Cluster	$l$ ( $^{\circ}$ )	$b$ ( $^{\circ}$ )	$N_{\text{member}}$	$N_{\text{BSS}}$	BSS Type / Features	Data / Instrument	Reference
Berkeley 39	223.5419	+10.0879	729	17	Single, Hot companion cand.	<i>Swift</i> /UVOT	Chand et al. (2024a)
King 2	122.8681	−04.6843	107	25	BSS+WD	<i>Astrosat</i> /UVIT	Jadhav et al. (2021)
M67	215.6893	+31.9256	1183	13	BSS+WD, Barium BSS	<i>Astrosat</i> /UVIT	Pandey et al. (2021)
Melotte 66	259.5807	−14.2625	1162	14	BSS+WD, Eclipsing Binary	<i>Swift</i> /UVOT	Rao et al. (2022a)
NGC 188	122.8404	+22.3804	3562	1	BSS+WD	UVIT, GALEX	Rani et al. (2021)
NGC 752	136.9070	−23.3032	223	15	BL, BSS+ELM WD	UVIT, UVOT	Jadhav et al. (2024)
NGC 2243	239.4799	−18.0105	889	12	BSS+WD, Single	<i>Swift</i> /UVOT	Sheikh & Medhi (2024a)
NGC 2420	198.1087	+19.6397	868	3	BSS+ELM WD	UVIT, UVOT	Yadav et al. (2024)
NGC 2506	230.5626	+09.9328	2175	9	BSS+WD (ELM/LM)	<i>Astrosat</i> /UVIT	Panthi et al. (2022)
NGC 2627	251.5777	+06.6531	422	4	BSS+ELM WD	<i>Astrosat</i> /UVIT	Saketh et al. (2024)
NGC 6791	069.9606	+10.9056	1654	47	BSS+WD, BSS+ELM WD	<i>Astrosat</i> /UVIT	Jadhav et al. (2023)
NGC 6940	069.8306	−07.1491	492	1	BSS+WD, BL	<i>Astrosat</i> /UVIT	Panthi & Vaidya (2024)
NGC 7142	105.3547	+09.4835	546	10	BSS+WD	UVIT, TESS	Panthi et al. (2024)
NGC 7789	115.5237	−05.3675	2800	16	BSS+ELM WD	<i>Astrosat</i> /UVIT	Vaidya et al. (2022b)

A key observational signature of the mass-transfer scenario is the presence of a hot white dwarf (WD) companion, which represents the remnant core of the original donor star. Identifying such companions is therefore central to constraining the evolutionary history of BSS systems. However, this task is challenging at optical wavelengths, where the luminous BSS primary overwhelms the faint WD’s flux. In contrast, WDs emit strongly in the ultraviolet (UV), where their presence can be inferred through a measurable UV excess. As a result, UV photometry has become an essential tool for confirming mass-transfer-origin BSS systems.

The presence of other blue stellar populations further complicates the identification of genuine BSSs in OCs. In addition to classical BSSs, blue lurkers, which are mass-transfer products that have not yet migrated to the canonical BSS region, can overlap with the main sequence (MS) in optical CMD (Leiner et al. 2019; Subramaniam et al. 2020). Similarly, morphologically defined blue plume stars may occupy regions close to the BSS locus. In this context, UV observations, combined with multi-wavelength SED analysis, are particularly effective for distinguishing true BSSs from contaminating populations (Gosnell et al. 2015; Sindhu et al. 2019a). Hot components, such as WDs and hot subdwarfs (sdB/sdO), produce distinct UV excesses that are not detectable in optical bands alone. While contamination in UV-selected samples is generally reduced, it cannot be entirely excluded.

In recent years, UV observations have significantly advanced the study of BSS populations in open clusters, particularly with *Astrosat*/UVIT (Singh et al. 2014; Tandon et al. 2017). As part of the UVIT Open Cluster Study (UOCS I–XIV), several works have identified WD companions in clusters such as M67, NGC 188, NGC 752, and NGC 6791 (e.g., Sindhu et al. 2018,

2019a; Jadhav et al. 2021, 2024). These studies demonstrated that high spatial resolution and multi-filter UV coverage are crucial for constructing reliable SEDs that can isolate hot compact components, including low-mass and hot post-mass-transfer remnants.

Recent UV studies with *Astrosat*/UVIT have therefore played a pivotal role in identifying hot companions to blue stragglers in several OCs (Subramaniam et al. 2016; Panthi & Vaidya 2024). However, these investigations are necessarily limited to targeted observations of a relatively small number of clusters. This naturally motivates the use of alternative UV facilities that provide broader sky coverage and more uniform datasets.

In this context, the *Swift* Ultraviolet/Optical Telescope (UVOT; Roming et al. 2000, 2005) offers a complementary approach. *Swift*/UVOT provides wide sky coverage, multiple UV filters, and a steadily growing archival database spanning many years. These characteristics make UVOT particularly well-suited for homogeneous studies across numerous clusters. Nevertheless, systematic assessments of BSS–WD systems based on UVOT photometry remain scarce in the literature. The current work represents one of the first systematic *Swift*/UVOT-based SED analyses of BSSs across numerous OCs, complementing existing UVIT investigations and expanding the observational basis for understanding mass-transfer products in low-density cluster environments.

In this work, we use *Swift*/UVOT archival data to systematically and homogeneously investigate the presence of hot companions to BSSs in OCs. By cross-matching a compilation of 502 known BSSs with 103 OCs observed by UVOT (Siegel et al. 2019), we identify 35 BSS candidates in nine OCs that have not previously been examined in the UV. For these targets, we construct multi-wavelength SEDs spanning the UV, optical, and

infrared regimes, and we test for the presence of hot compact companions by comparing single-star models with binary composite models. We detect significant UV excesses in 15 of the 35 systems, consistent with WD companions, and derive their physical parameters, classifying them as low-mass or hot WDs.

## 2. DATA

To comprehensively characterize the physical properties of BSSs and reveal their potential hot companions, we compiled a multi-wavelength dataset spanning the ultraviolet (UV) to the mid-infrared (MIR). This extensive photometric coverage combines high-sensitivity UV observations from *Swift*/UVOT with precision optical photometry and astrometry from Gaia DR3 (Gaia Collaboration et al. 2023), complemented by ground-based surveys and infrared data from Two Micron All Sky Survey (2MASS; Skrutskie et al. 2006) and Wide-field Infrared Survey Explorer (WISE; Wright et al. 2010). By integrating these diverse data sources, we constructed robust SEDs essential for determining stellar parameters and detecting flux excesses indicative of binary systems. The normalized transmission curves and spectral coverage of the photometric passbands adopted in this analysis are shown in Figure 1.

### 2.1. Ultraviolet (UV) Observations

Detecting the faint thermal emission from hot, sub-luminous companions requires high-sensitivity observations in the ultraviolet regime, where these objects emit a substantial fraction of their flux. To achieve this, we utilized data from the *Swift*/UVOT aboard the Neil Gehrels Swift Observatory (Gehrels et al. 2004). The UVOT, a modified 30 cm Ritchey-Chrétien telescope with a  $17' \times 17'$  field of view, provides the critical Near-UV (NUV) and Far-UV (FUV) coverage needed for our analysis. Specifically, we focused on photometry from the *UVM2* ( $\lambda_{\text{eff}} \approx 2246 \text{ \AA}$ ) and *UVW2* ( $\lambda_{\text{eff}} \approx 2086 \text{ \AA}$ ) filters (Breeveld et al. 2011). Rather than performing a custom reduction of raw imagery, we leveraged the high-level science products available in the *Swift*/UVOT Archive<sup>8</sup>. We adopted the calibrated flux values from the cluster point-source catalogs generated by Siegel et al. (2019), thereby ensuring robust background subtraction and coincidence-loss corrections. A summary of the UVOT observations for the clusters in our sample is provided in Table 2.

<sup>8</sup> <https://archive.stsci.edu/hlsp/uvot-oc>

**Table 2.** Log of *Swift*/UVOT observations. The columns list the total exposure times for the filters.

ID	Cluster	Exposure (s)		
		<i>UVW2</i>	<i>UVM2</i>	<i>UVW1</i>
1	Berkeley 29	3151	2027	1665
2	Berkeley 31	1951	2083	2123
3	Berkeley 37	1644	1644	1511
4	Berkeley 75	5158	697	370
5	NGC 2192	1797	1797	2003
6	NGC 2204	974	1923	–
7	NGC 2360	1881	1881	1905
8	NGC 2533	2132	1768	1718
9	NGC 6939	3992	3992	3968

### 2.2. Optical Photometry and Astrometry

The foundational optical data for this study were derived from the Gaia mission’s third Data Release (Gaia Collaboration et al. 2023). *Gaia* DR3 database provides the precise astrometric parameters ( $\alpha$ ,  $\delta$ ,  $\varpi$ ,  $\mu_\alpha \cos \delta$ ,  $\mu_\delta$ ) essential for establishing robust cluster membership. We also utilized its high-precision photometry in the *G* ( $\lambda_{\text{eff}} \approx 673 \text{ nm}$ ), *G<sub>BP</sub>* ( $\lambda_{\text{eff}} \approx 532 \text{ nm}$ ), and *G<sub>RP</sub>* ( $\lambda_{\text{eff}} \approx 797 \text{ nm}$ ) passbands. To construct comprehensive SEDs covering the full optical window, we complemented the *Gaia* data with ground-based surveys. We retrieved broadband photometry ( $g, r, i, z, y$ ) from the Pan-STARRS1 Data Release 2 (DR2; Flewelling et al. 2020). For southern targets, we extended our coverage using the SkyMapper Southern Survey (SMSS; Keller et al. 2007) Data Release 4 ( $u, v, g, r, i, z$ ) (Onken et al. 2024).

### 2.3. Infrared (IR) Archival Data

To constrain the Rayleigh-Jeans tail of the stellar SEDs, we incorporated archival data from near infrared (NIR) and MIR surveys. NIR magnitudes in the *J* ( $1.24 \mu\text{m}$ ), *H* ( $1.66 \mu\text{m}$ ), and *K<sub>s</sub>* ( $2.16 \mu\text{m}$ ) bands were sourced from the 2MASS (Skrutskie et al. 2006). For the MIR regime, we utilized photometry from the AllWISE data release of the WISE (Cutri et al. 2021). Our analysis prioritized the *W1* ( $3.35 \mu\text{m}$ ) and *W2* ( $4.60 \mu\text{m}$ ) bands because of their superior signal-to-noise ratios relative to the longer-wavelength channels. Finally, all multi-wavelength photometric data were ingested into the Virtual Observatory SED Analyzer<sup>9</sup> (VOSA; Bayo et al. 2008) to perform the SED fitting procedures described in the subsequent sections.

<sup>9</sup> <https://svo2.cab.inta-csic.es/theory/vosa>

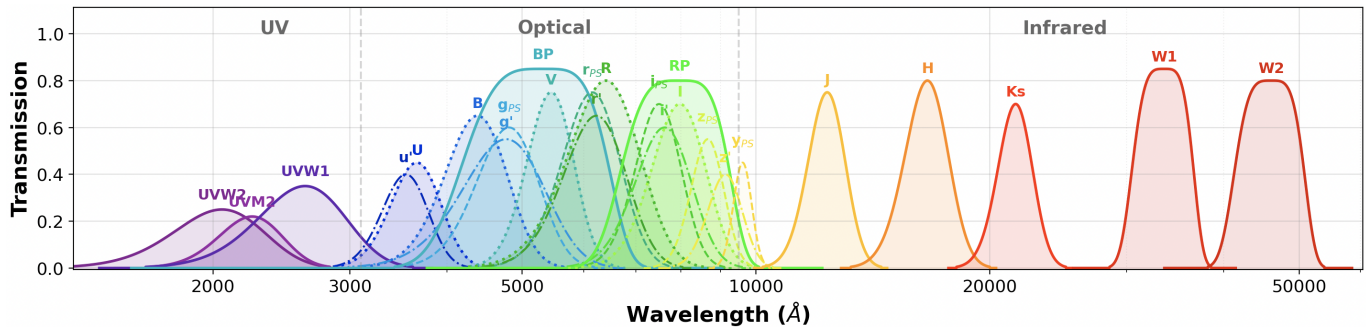


**Figure 1.** Normalized transmission curves for the photometric passbands adopted in the SED fitting. The coverage extends from the ultraviolet to the infrared regime.

### 3. METHOD

#### 3.1. Sample Selection

To construct a comprehensive sample of BSSs suitable for UV analysis, we utilized the archival data from the *Swift*/UVOT. The sample selection process is summarized in Figure 2. We began by cross-correlating two primary datasets: a catalog of 502 OCs known to host BSS populations (e.g., Qin et al. 2026; Li et al. 2023; Rain et al. 2024, 2021; Jadhav & Subramaniam 2021; Ahumada & Lapasset 2007) and the list of 103 OCs available in the *Swift* archive (Siegel et al. 2019). This initial cross-match yielded 31 common OCs that possess both identified BSS candidates and available archival UV observations.

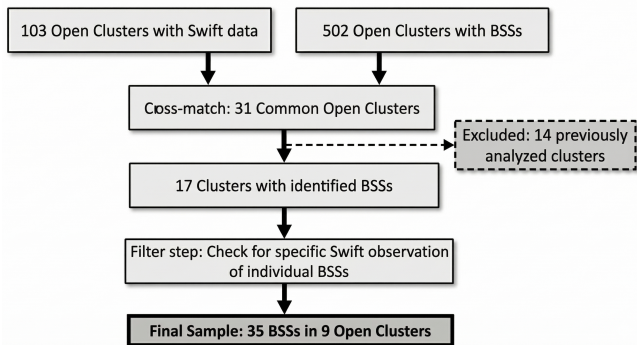


**Figure 2.** Flowchart of the sample selection procedure.

To ensure the novelty of our analysis and to avoid duplicating results, we conducted a literature review of these 34 OCs. We excluded 14 OCs that had been previously analyzed using *Swift*/UVOT or *Astrosat*/UVIT data in recent studies. This filtering step yielded a subset of 17 candidate clusters, containing 47 identified BSS candidates.

Finally, we visually inspected the available *Swift* images and checked the exposure times for each of the 47 candidates to ensure sufficient data quality for photometric analysis. In several cases, the BSS candidates

fell outside the instrument’s field of view or lacked observations in the required filters. Consequently, our final sample comprises 35, distributed across nine OCs.

To further validate the membership status and evolutionary state of our final sample, we cross-matched the 35 candidates and their host clusters against the comprehensive OCs catalog of Hunt & Reffert (2024). This catalog provides high-precision astrometric data and robust membership probabilities derived from Gaia DR3. Using these membership probabilities, we constructed the CMDs presented in Figure 3. We note that the horizontal dashed line marks an approximate MSTO magnitude used to separate MS and evolved stars, and should not be taken as a strict boundary for BSS identification.

#### 3.2. SED Analysis

To determine the fundamental physical properties ( $T_{\text{eff}}$ ,  $R$ ,  $L$ ) of the BSS candidates, and to screen for potential unresolved hot companions, we performed a detailed SED analysis. We employed the VOSA to construct and fit SEDs using a broad photometric baseline. The dataset covers the ultraviolet (*Swift*/UVOT), optical (*Gaia* DR3, Pan-STARRS, SkyMapper, TESS), and infrared (2MASS, WISE) regimes, as detailed in Section 2.

For the fitting process, we provided VOSA with the equatorial coordinates of the sources, along with cluster distances ( $d_{\text{geo}}$ ) adopted from the Gaia EDR3-based geometric distance estimates of Bailer-Jones et al. (2021). These distances account for the non-linearity of the parallax distance transformation and incorporate a physically motivated Galactic prior, making them more robust than simple parallax inversions, particularly for distant and low-parallax cluster members. VOSA then retrieved the available multiwavelength photometry within a  $3''$  search radius around each source. A similar approach has been adopted in previous VOSA-based SED studies of BSS populations in OCs (Chand et al. 2024a,b; Sheikh & Medhi 2024a,b). To ensure data integrity, we visually inspected each source using

**Table 3.** Properties of the 35 candidates in the selected nine OCs. The columns list the Cluster name, Gaia DR3 Source ID, and the observed fluxes (in  $\text{erg s}^{-1} \text{cm}^{-2} \text{\AA}^{-1}$ ) with uncertainties for the *Swift*/UVOT *UVW2*, *UVM2*, and *UVW1* filters.

BSS ID	Cluster	Gaia DR3 ID	Observed Flux ( $\text{erg s}^{-1} \text{cm}^{-2} \text{\AA}^{-1}$ )		
			<i>UVW2</i>	<i>UVM2</i>	<i>UVW1</i>
BSS 01	Berkeley 29	3358218745306932224	$1.80\text{E-17} \pm 3.24\text{E-17}$	$1.75\text{E-17} \pm 5.95\text{E-17}$	$2.10\text{E-17} \pm 5.41\text{E-17}$
BSS 02	Berkeley 31	3157241012027949568	$1.93\text{E-16} \pm 1.42\text{E-17}$	$2.00\text{E-17} \pm 1.66\text{E-17}$	$2.47\text{E-16} \pm 2.95\text{E-17}$
BSS 03	Berkeley 31	3157241115107807872	$5.12\text{E-18} \pm 8.49\text{E-18}$	$5.48\text{E-18} \pm 7.06\text{E-18}$	$6.63\text{E-18} \pm 7.32\text{E-18}$
BSS 04	Berkeley 31	3157241282608500096	$2.13\text{E-17} \pm 5.70\text{E-18}$	$2.46\text{E-18} \pm 5.45\text{E-18}$	$3.09\text{E-17} \pm 5.97\text{E-18}$
BSS 05	Berkeley 31	3157241355625967744	$1.55\text{E-17} \pm 1.57\text{E-17}$	$1.62\text{E-17} \pm 1.49\text{E-17}$	$1.88\text{E-17} \pm 2.08\text{E-17}$
BSS 06	Berkeley 31	3157241523126689536	$4.68\text{E-17} \pm 1.12\text{E-17}$	$4.91\text{E-18} \pm 9.49\text{E-18}$	$6.21\text{E-17} \pm 1.37\text{E-17}$
BSS 07	Berkeley 31	3157241557486428160	$3.86\text{E-17} \pm 9.59\text{E-18}$	$4.05\text{E-18} \pm 6.72\text{E-18}$	$4.73\text{E-18} \pm 7.85\text{E-18}$
BSS 08	Berkeley 31	3157238263249488256	$2.43\text{E-17} \pm 7.83\text{E-18}$	$3.24\text{E-17} \pm 6.96\text{E-18}$	$4.69\text{E-17} \pm 6.04\text{E-17}$
BSS 09	Berkeley 31	3157241351327999104	$1.09\text{E-17} \pm 3.60\text{E-18}$	$1.36\text{E-18} \pm 3.75\text{E-18}$	$1.78\text{E-17} \pm 4.75\text{E-18}$
BSS 10	Berkeley 31	3157241527424009216	$1.95\text{E-17} \pm 5.75\text{E-18}$	$2.18\text{E-17} \pm 5.22\text{E-18}$	$3.60\text{E-17} \pm 7.29\text{E-18}$
BSS 11	Berkeley 31	3157241561783738496	$1.74\text{E-17} \pm 4.98\text{E-18}$	$1.84\text{E-17} \pm 4.41\text{E-18}$	$3.45\text{E-17} \pm 4.69\text{E-18}$
BSS 12	Berkeley 31	3157242283338251648	$1.78\text{E-17} \pm 4.77\text{E-18}$	$2.08\text{E-17} \pm 3.65\text{E-18}$	$2.79\text{E-17} \pm 5.65\text{E-18}$
BSS 13	Berkeley 37	3109976821085220736	$3.34\text{E-16} \pm 4.31\text{E-16}$	$2.92\text{E-16} \pm 3.23\text{E-16}$	$2.48\text{E-16} \pm 2.28\text{E-16}$
BSS 14	Berkeley 75	2922222806776944640	$2.83\text{E-17} \pm 2.03\text{E-17}$	$2.02\text{E-17} \pm 1.36\text{E-17}$	–
BSS 15	Berkeley 75	2922223253455323904	$8.11\text{E-17} \pm 1.05\text{E-17}$	$7.53\text{E-17} \pm 1.87\text{E-17}$	$7.83\text{E-17} \pm 2.02\text{E-17}$
BSS 16	Berkeley 75	2922222806776944640	$1.91\text{E-17} \pm 1.46\text{E-17}$	–	–
BSS 17	Berkeley 75	2922223249154669440	$9.61\text{E-17} \pm 2.83\text{E-17}$	$9.37\text{E-17} \pm 7.42\text{E-17}$	$1.47\text{E-16} \pm 7.98\text{E-17}$
BSS 18	NGC 2192	959419037352088960	$2.38\text{E-17} \pm 2.41\text{E-17}$	$2.06\text{E-17} \pm 2.47\text{E-17}$	$2.84\text{E-17} \pm 2.36\text{E-17}$
BSS 19	NGC 2192	959442852947148672	$1.00\text{E-17} \pm 8.29\text{E-18}$	$9.90\text{E-18} \pm 8.21\text{E-18}$	$1.45\text{E-17} \pm 1.07\text{E-17}$
BSS 20	NGC 2204	2941920110907962624	$4.30\text{E-17} \pm 1.70\text{E-17}$	–	–
BSS 21	NGC 2204	2941922928406484864	$4.42\text{E-17} \pm 1.26\text{E-17}$	$4.75\text{E-17} \pm 1.23\text{E-17}$	–
BSS 22	NGC 2204	2941936259984685312	$1.45\text{E-16} \pm 2.14\text{E-16}$	$1.35\text{E-16} \pm 1.49\text{E-16}$	–
BSS 23	NGC 2204	2941936741021002240	$8.39\text{E-17} \pm 8.50\text{E-17}$	$7.79\text{E-17} \pm 7.89\text{E-17}$	–
BSS 24	NGC 2204	2941939283641661056	$9.80\text{E-16} \pm 1.54\text{E-16}$	$9.49\text{E-16} \pm 1.40\text{E-16}$	–
BSS 25	NGC 2204	2941939283641661568	$1.21\text{E-16} \pm 2.56\text{E-16}$	$1.20\text{E-16} \pm 1.88\text{E-16}$	–
BSS 26	NGC 2204	2941935847667840128	$3.23\text{E-17} \pm 1.04\text{E-17}$	$3.54\text{E-17} \pm 1.44\text{E-17}$	$8.47\text{E-17} \pm 8.58\text{E-17}$
BSS 27	NGC 2204	2941936191265206016	$3.26\text{E-17} \pm 3.90\text{E-17}$	$3.07\text{E-17} \pm 3.11\text{E-17}$	$3.60\text{E-17} \pm 3.32\text{E-17}$
BSS 28	NGC 2204	2941939386720881536	$5.15\text{E-17} \pm 1.80\text{E-17}$	$5.91\text{E-17} \pm 1.52\text{E-17}$	$1.14\text{E-17} \pm 1.47\text{E-17}$
BSS 29	NGC 2360	3031253334726488576	$7.29\text{E-17} \pm 5.37\text{E-17}$	$6.32\text{E-17} \pm 5.24\text{E-17}$	$9.34\text{E-17} \pm 5.16\text{E-17}$
BSS 30	NGC 2533	5596625961920878848	$5.23\text{E-17} \pm 3.37\text{E-17}$	$4.17\text{E-17} \pm 3.46\text{E-17}$	$7.63\text{E-17} \pm 4.22\text{E-17}$
BSS 31	NGC 6939	2194727330484552960	$1.12\text{E-16} \pm 1.03\text{E-16}$	$8.24\text{E-17} \pm 1.14\text{E-17}$	$1.48\text{E-16} \pm 1.23\text{E-16}$
BSS 32	NGC 6939	2194728120758530944	$5.58\text{E-16} \pm 6.68\text{E-18}$	$3.84\text{E-16} \pm 5.30\text{E-18}$	$9.94\text{E-16} \pm 1.01\text{E-17}$
BSS 33	NGC 6939	2194818899185893760	$2.11\text{E-16} \pm 5.04\text{E-17}$	$1.21\text{E-16} \pm 3.35\text{E-17}$	$3.98\text{E-16} \pm 5.13\text{E-17}$
BSS 34	NGC 6939	2194724856583515776	$2.11\text{E-16} \pm 5.04\text{E-17}$	$1.21\text{E-16} \pm 3.35\text{E-17}$	$3.98\text{E-16} \pm 5.13\text{E-17}$
BSS 35	NGC 6939	2194724959662728064	$1.12\text{E-16} \pm 1.03\text{E-16}$	$8.24\text{E-17} \pm 1.14\text{E-17}$	$1.48\text{E-16} \pm 1.23\text{E-16}$

Aladin<sup>10</sup> and confirmed that the photometry was free from contamination by nearby sources. We applied extinction corrections using the  $R_V = 3.1$  reddening laws of Fitzpatrick (1999) and Indebetouw et al. (2005).

We initially modeled the SEDs using single-star atmospheres from the Kurucz ODFNEW/NOVER grid (Castelli et al. 1997; Castelli & Kurucz 2003). The parameter space was restricted to temperatures between 5000–15000 K and surface gravities of  $\log g = 2.5$ –5.0 dex, with metallicities fixed to literature-based cluster values (e.g., Casamiquela et al. 2019; Donor et al. 2020; Dias et al. 2021; Randich et al. 2022; Fu et al. 2022; Netopil et al. 2022). The quality of the fit was assessed using the visual goodness-of-fit parameter,  $V_{\text{gfb}}$

(Bayo et al. 2008). To account for potentially underestimated photometric errors, VOSA calculates a modified reduced  $\chi^2$  where flux errors are enforced to be at least 10% of the observed flux. Following established conventions (e.g., Jiménez-Esteban et al. 2018; Zeng et al. 2025), we considered fits with  $V_{\text{gfb}} < 10$ –15 to be reliable representations of single stars (Rebassa-Mansergas et al. 2021). Figure 4 displays the SED analysis for a representative single BSS in NGC 2204. The corresponding fits for all other single stars in our sample can be found in Appendix A.

The uncertainties in the derived radii and luminosities were estimated through standard error propagation within the VOSA framework. The stellar radius is obtained from the scaling factor  $M_d = (R/d)^2$ , where  $d$  is the cluster distance, giving  $R = d\sqrt{M_d}$ . Its uncertainty

<sup>10</sup> <https://aladin.u-strasbg.fr/>

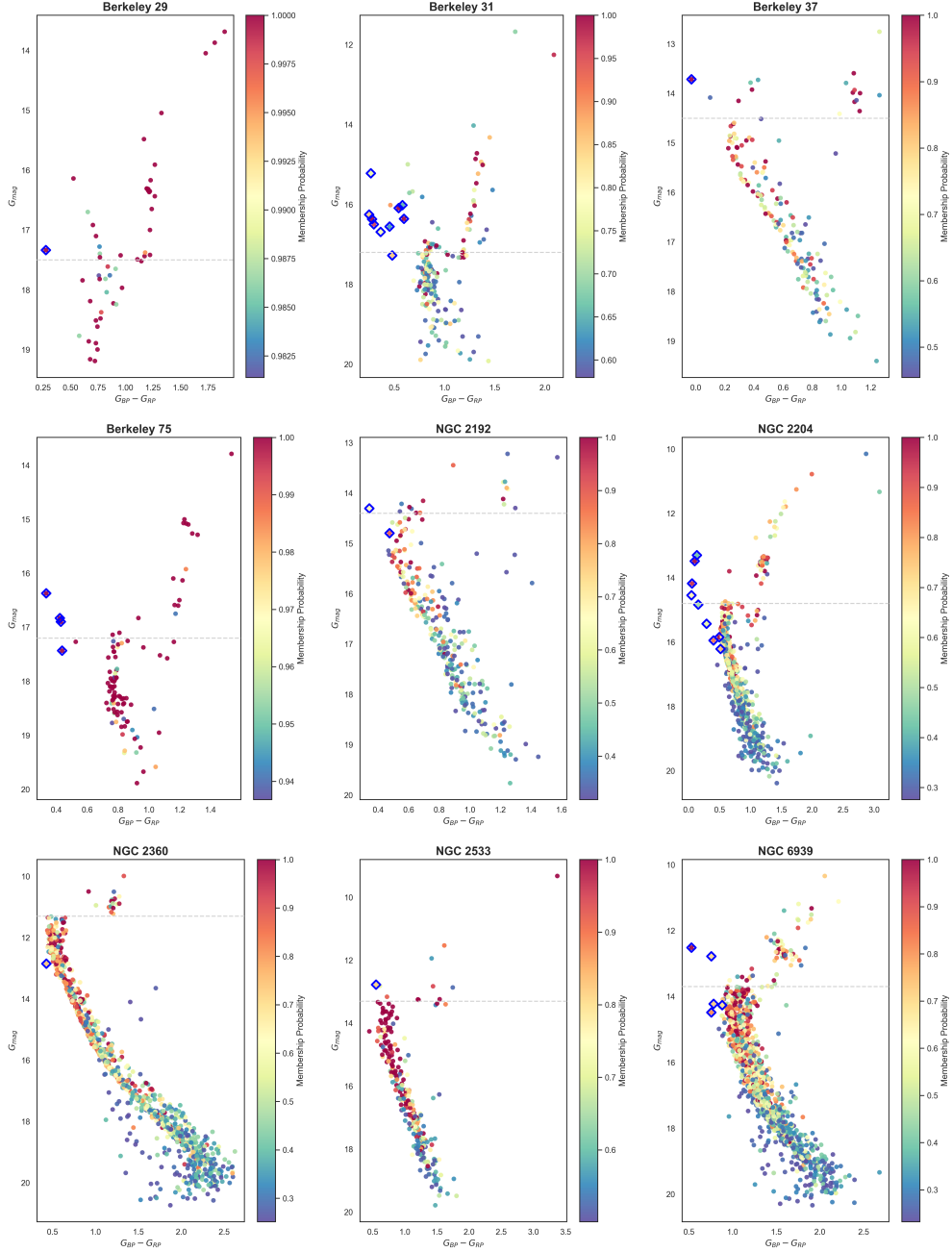


**Figure 3.** CMDs for the studied nine OCs, showing the the  $G$ -band apparent magnitude versus  $G_{BP} - G_{RP}$  color. The plotted stars correspond to cluster members adopted from [Hunt & Reffert \(2024\)](#), and the color scale indicates their associated membership probabilities, with redder colors denoting higher membership likelihood. Blue diamond symbols mark the identified BSS candidates with available *Swift*/UVOT observations in each cluster. The horizontal dashed line represents the adopted MSTO magnitude in this study.

is:

$$\sigma_R = R \cdot \sqrt{\left(\frac{\sigma_d}{d}\right)^2 + \frac{1}{4} \left(\frac{\sigma_{M_d}}{M_d}\right)^2}, \quad (1)$$

where  $\sigma_d$  and  $\sigma_{M_d}$  are the uncertainties in distance ([Bailer-Jones et al. 2021](#)) and scaling factor, respectively. The luminosity is computed from  $L = 4\pi R^2 \sigma T_{\text{eff}}^4$ ,

with uncertainty ([Eker et al. 2015, 2018, 2024](#)):

$$\frac{\sigma_L}{L} = \sqrt{\left(\frac{2\sigma_R}{R}\right)^2 + \left(\frac{4\sigma_{T_{\text{eff}}}}{T_{\text{eff}}}\right)^2}. \quad (2)$$

The temperature uncertainties were estimated via Monte Carlo simulations, in which the observed photometric fluxes were perturbed within their measurement

**Table 4.** Fundamental parameters of the nine OCs adopted from [Hunt & Reffert \(2024\)](#). The columns list equatorial coordinates, proper-motion components, and trigonometric parallax, radial velocity, logarithmic age,  $V$ -band extinction, distance modulus, and half-mass relaxation time. The relaxation times are computed as described in [Section 4.2.1](#).

No.	Cluster	$\alpha_{2000}$ (hh:mm:ss)	$\delta_{2000}$ (dd:mm:ss)	$\mu_{\alpha} \cos \delta$ (mas yr $^{-1}$ )	$\mu_{\delta}$ (mas yr $^{-1}$ )	$\varpi$ (mas)	RV (km s $^{-1}$ )	$\log t$ (yr)	$A_V$ (mag)	$(m - M)$ (mag)	$t_{\text{relax}}$ (Myr)
1	Berkeley 29	06:53:03.81	+16:55:33.16	+0.12 $\pm$ 0.10	-1.06 $\pm$ 0.05	0.05 $\pm$ 0.05	25.39 $\pm$ 0.18	8.41 $\pm$ 0.62	1.49 $\pm$ 0.78	15.60 $\pm$ 0.10	4
2	Berkeley 31	06:57:37.61	+08:17:17.29	+0.11 $\pm$ 0.13	-0.92 $\pm$ 0.09	0.12 $\pm$ 0.08	65.27 $\pm$ 5.06	9.08 $\pm$ 0.23	0.43 $\pm$ 0.21	13.90 $\pm$ 0.19	17
3	Berkeley 37	07:20:16.54	-00:59:53.55	-1.05 $\pm$ 0.06	+0.71 $\pm$ 0.07	0.18 $\pm$ 0.05	81.75 $\pm$ 3.79	9.01 $\pm$ 0.19	0.07 $\pm$ 0.06	13.51 $\pm$ 0.22	13
4	Berkeley 75	06:48:59.75	-23:59:45.57	-0.24 $\pm$ 0.07	+1.18 $\pm$ 0.11	0.11 $\pm$ 0.07	125.07 $\pm$ 1.81	9.27 $\pm$ 0.21	0.20 $\pm$ 0.16	14.36 $\pm$ 0.22	17
5	NGC 2192	06:15:17.39	+39:50:33.94	+0.19 $\pm$ 0.05	-1.97 $\pm$ 0.06	0.23 $\pm$ 0.05	20.75 $\pm$ 5.53	9.03 $\pm$ 0.19	0.19 $\pm$ 0.11	13.08 $\pm$ 0.19	13
6	NGC 2204	06:15:32.45	-18:40:17.37	-0.58 $\pm$ 0.06	+1.96 $\pm$ 0.07	0.20 $\pm$ 0.05	93.89 $\pm$ 1.42	9.26 $\pm$ 0.17	0.05 $\pm$ 0.05	13.29 $\pm$ 0.22	76
7	NGC 2360	07:17:45.75	-15:38:39.91	+0.39 $\pm$ 0.14	+5.63 $\pm$ 0.13	0.92 $\pm$ 0.05	27.25 $\pm$ 0.73	9.16 $\pm$ 0.18	0.12 $\pm$ 0.08	10.02 $\pm$ 0.17	36
8	NGC 2533	08:07:04.48	-29:51:37.53	-3.18 $\pm$ 0.09	+5.07 $\pm$ 0.08	0.35 $\pm$ 0.05	40.58 $\pm$ 5.16	8.86 $\pm$ 0.18	0.83 $\pm$ 0.19	12.04 $\pm$ 0.16	27
9	NGC 6939	20:31:36.36	+60:39:04.76	-1.82 $\pm$ 0.10	-5.46 $\pm$ 0.10	0.53 $\pm$ 0.03	-18.81 $\pm$ 1.12	9.02 $\pm$ 0.15	1.33 $\pm$ 0.18	11.32 $\pm$ 0.14	28

errors, and the SED fitting was repeated over multiple realizations; the dispersion in  $T_{\text{eff}}$  was adopted as the  $1\sigma$  uncertainty. As a result, the temperature uncertainties vary between sources, largely reflecting differences in photometric quality and wavelength coverage. The similar uncertainty levels in radius and luminosity are mainly driven by the shared fractional distance error, which is expected to contribute significantly to the radius uncertainty for members of the same cluster.

A critical component of our analysis was the search for UV excesses, which often betray the presence of a WD companion ([Gosnell et al. 2015](#); [Rao et al. 2022b](#)). We analyzed the fractional residuals between the observed and model fluxes, specifically in the *Swift*/UVOT filters. Sources exhibiting a residual excess greater than  $\sim 30\%$  in at least two UV bands were flagged as binary candidates ([Chand et al. 2024b](#)). A UV excess of  $\geq 30\%$  in at least two UV bands is required to ensure that the detected excesses are robust against photometric uncertainties and small extinction mismatches. This threshold is chosen to minimize contamination from photometric uncertainties and extinction mismatches while ensuring robust identification of genuine excess emission. Similar multi-band UV-excess criteria have been employed in previous UV studies of blue stragglers and post-mass-transfer systems, where they have reliably identified hot, compact companions ([Gosnell et al. 2015](#); [Vaidya et al. 2022b](#); [Chand et al. 2024b](#)).

For candidates showing a significant UV excess, we used the VOSA Binary Fit module. These systems were modeled as a combination of a cool BSS component ([Castelli & Kurucz 2003](#)) and a hot companion, represented by WD models ([Koester 2010](#)), with parameters ranging from  $T_{\text{eff,WD}} = 10,000$  to  $80,000$  K and  $\log g_{\text{WD}} = 6.5$  to  $9.5$  dex. The parameters for both components were optimized simultaneously.

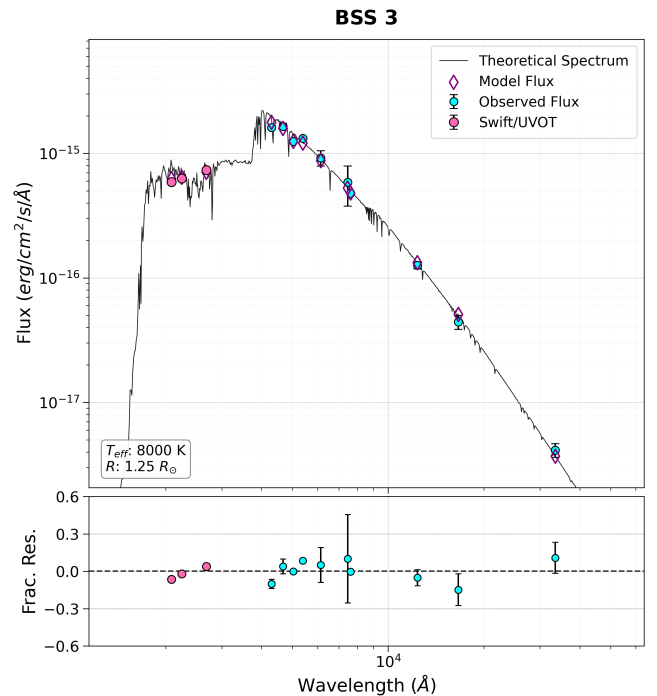


**Figure 4.** Representative SED fitting analysis for a single-component BSS candidate in Berkeley 31. **Top panel:** Cyan circles with error bars denote extinction-corrected observed multi-wavelength photometric fluxes. The solid black curve represents the best-fitting theoretical spectrum derived from [Castelli et al. \(1997\)](#) models. Purple diamonds indicate the synthetic fluxes integrated over the corresponding pass-bands. **Bottom panel:** The fractional residuals between the observed data and the model fluxes, demonstrating the quality of the fit. The SED plots for the remaining single-component BSS candidates are presented in [Appendix A](#).

In addition to these cases, we identify BSS 28 as a source exhibiting a noticeable IR excess. Such excess emission may be indicative of circumstellar material, including possible dust or debris disk structures ([Patel](#)

et al. 2014). However, mid-infrared excesses derived from broadband photometry can be affected by background contamination, blending, or photometric uncertainties, especially in crowded cluster fields. Therefore, the nature of the excess in BSS 28 cannot be conclusively established with the current data. Therefore, we consider BSS 28 a tentative candidate, and its detailed characterization will require higher-quality, higher-resolution infrared observations in future studies.

We note that SED fitting of composite systems is subject to intrinsic degeneracies between effective temperature and radius, especially for hot compact companions. The inclusion of UV data, in particular, reduces these degeneracies, as the UV flux is highly sensitive to the temperature of the hot component while contributing negligibly at optical wavelengths. As a result, the derived parameters for the hot companions, particularly in systems with strong UV excesses, are reasonably well constrained; however, they remain subject to degeneracies and should be interpreted with caution in the absence of spectroscopic constraints.

We note that the derived parameters for BSS 15, BSS 30, and BSS 32 remain comparatively uncertain because these systems lack strong FUV constraints. In such cases, the decomposition of the composite SED is more strongly affected by degeneracies between the temperature and radius of the hot component. Therefore, the inferred parameters for these systems should be interpreted with caution until deeper ultraviolet observations or spectroscopic follow-up data become available.

#### 4. RESULTS AND DISCUSSION

In this section, we present the results of the multi-wavelength SED analysis performed on 35 candidates across nine OCs. One of the key outcomes of this study is the identification of candidate hot WD companions in several systems within our sample. These hot, compact components provide important observational constraints on the mass-transfer formation channel and are typically obscured at optical wavelengths by the BSS primary’s dominant luminosity. However, the high UV sensitivity and broad spectral coverage provided by the *Swift*/UVOT observations enabled the detection and characterization of these faint companions.

Our analysis shows that the majority of the BSS sample (20 out of 35 targets) consists of systems whose additional components cannot be resolved or detected within the sensitivity limits of the current dataset, rather than being conclusively single stars. Among the remaining systems, 15 objects ( $\sim 43\%$ ) exhibit ultraviolet excesses indicative of potential hot companions. We further examine whether the fraction of binary BSSs identified in

each cluster depends on global cluster properties, particularly the overall binary fraction. However, homogeneous estimates of cluster-wide binary fractions are not available for all targets in our sample, which prevents a direct quantitative comparison. Instead, we perform a qualitative assessment of the relative occurrence of UV-excess BSSs across clusters. Clusters with larger BSS populations tend to exhibit a higher number of candidate binary systems, primarily reflecting sample-size effects rather than an intrinsic physical correlation. Therefore, while our results are consistent with a binary-driven formation scenario, a robust test of any correlation between the cluster binary fraction and BSS binarity will require homogeneous measurements of binary fractions from spectroscopic or variability studies. In the following subsections, we present the fundamental physical parameters ( $T_{\text{eff}}$ ,  $R$ , and  $L$ ) derived for both single and binary systems and discuss the implications of these newly discovered binaries for the evolutionary history of BSS.

We present the fundamental physical parameters ( $T_{\text{eff}}$ ,  $R$ , and  $L$ ) derived for the 35 candidates in our sample. As outlined in Section 3.2, we constructed comprehensive multi-wavelength SEDs by anchoring our dataset with *Swift*/UVOT photometry. To rigorously constrain the stellar properties, observed fluxes were fitted against theoretical atmosphere models using the VOSA framework. We employed Kurucz ODFNEW/NOVER grids (Castelli et al. 1997) to model the BSS primaries. For targets exhibiting significant UV excesses, a strong indicator of binarity, we adopted a two-component fitting strategy, combining the cool stellar model with hot WD spectra from Koester (2010). The final adopted parameters, along with uncertainties estimated via Monte Carlo simulations to account for photometric and distance errors, are listed in Table 5. Additionally, representative SEDs for four binary BSS systems are shown in Figure 5.

Our methodology aligns with and expands upon recent studies by Sheikh & Medhi (2024b) and Zeng et al. (2025), confirming the efficacy of combining Gaia DR3 astrometry with broad-band photometry for characterizing BSS populations. Despite differences in cluster environments, ranging from the old, metal-poor NGC 2243 to the younger NGC 6134, both studies independently concluded that binary mass transfer is a dominant formation pathway. While Sheikh & Medhi (2024b) successfully identified post-mass-transfer systems hosting hot WD companions, Zeng et al. (2025) detected active mass-transfer phases (EA-type binaries). Building on this robust multi-wavelength framework, our analysis extends to a diverse sample of nine OCs, leveraging

**Table 5.** Results of the two-component SED fitting analysis, showing the derived parameters for the binary BSS candidates. The columns list the host cluster, Gaia DR3 source identifier, and equatorial coordinates ( $\alpha$ ,  $\delta$ ). For each binary component (designated A = primary, B = secondary companion), the derived fundamental parameters are provided: effective temperature ( $T_{\text{eff}}$ ), radius ( $R$ ), and luminosity ( $L$ ). Finally, the scaling factors, the number of photometric points used in the fit ( $N_{\text{fit}}$ ), reduced chi-square ( $\chi^2_{\nu}$ ), the goodness-of-fit metric (vgf and vgf<sub>b</sub>) are presented.

BSS ID	Cluster	$\alpha$	$\delta$	Comp.	$T_{\text{eff}}$	$R$	$L$	Scaling Factor	$N_{\text{fit}}$	$\chi^2_{\nu}$	vgf	vgf <sub>b</sub>
BSS 06	Berkeley 31	06:57:37.44	+08:17:16.8	A	8000±121	1.45±0.09	7.71±0.79	3.69E-23	20	4.35	9.46	0.65
				B	15500±125	0.20±0.01	2.08±0.21	7.08E-25				
BSS 07	Berkeley 31	06:57:40.56	+08:17:45.6	A	8000±150	1.60±0.10	9.47±0.97	3.49E-23	20	3.09	7.56	1.18
				B	15250±125	0.12±0.01	0.72±0.07	2.01E-25				
BSS 10	Berkeley 31	06:57:36.24	+08:17:24.0	A	7000±177	1.37±0.09	4.06±0.42	7.63E-23	18	1.74	9.27	2.51
				B	15250±125	0.07±0.01	0.22±0.02	1.81E-25				
BSS 14	Berkeley 75	06:49:00.24	-23:59:52.8	A	8250±221	1.31±0.08	7.13±0.73	3.29E-23	14	5.51	6.8	0.77
				B	45000±2500	0.03±0.01	3.67±0.37	3.86E-26				
BSS 15	Berkeley 75	06:49:00.72	-24:00:50.4	A	10000±178	1.53±0.05	21.07±1.44	3.31E-23	18	6.98	14.21	0.99
				B	45000±2500	0.06±0.01	16.76±1.12	1.34E-25				
BSS 17	Berkeley 75	06:49:00.00	-23:59:56.4	A	7500±148	1.52±0.09	6.58±0.68	3.74E-23	15	7.09	21.08	2.09
				B	15250±125	0.20±0.01	2.01±0.21	6.79E-25				
BSS 18	NGC 2192	06:15:19.94	+39:48:56.9	A	8250±204	3.03±0.18	38.44±3.93	3.01E-22	19	15.25	34.27	2.24
				B	15500±125	0.37±0.02	7.22±0.73	4.50E-24				
BSS 19	NGC 2192	06:15:30.07	+39:52:57.4	A	8250±185	2.71±0.16	30.58±3.08	2.29E-22	19	18.09	37.41	2.01
				B	17250±125	0.31±0.02	7.80±0.78	3.07E-24				
BSS 20	NGC 2204	06:15:52.32	-18:45:21.6	A	7500±125	4.82±0.41	66.30±10.41	7.36E-22	24	19.12	18.98	3.42
				B	15000±125	0.24±0.02	2.71±0.42	1.93E-24				
BSS 21	NGC 2204	06:15:30.24	-18:38:45.6	A	7500±123	1.43±0.09	5.86±0.60	7.56E-23	23	8.28	16.27	3.36
				B	15250±125	0.08±0.01	0.30±0.03	2.25E-25				
BSS 25	NGC 2204	06:15:25.68	-18:38:38.4	A	7250±135	2.29±0.14	13.01±1.33	1.04E-22	21	14.9	14.01	2.34
				B	40000±1750	0.02±0.01	1.08±0.11	1.44E-26				
BSS 28	NGC 2204	06:15:54.72	-18:50:45.6	A	7750±125	1.94±0.19	12.29±2.23	9.37E-23	25	6.00	19.05	1.58
				B	50000±3750	0.03±0.01	3.64±0.65	4.17E-26				
BSS 29	NGC 2360	07:17:48.00	-15:42:10.8	A	7750±160	1.61±0.10	8.38±0.93	1.28E-21	23	26.25	22.01	1.02
				B	45000±2500	0.02±0.01	1.21±0.12	3.20E-25				
BSS 30	NGC 2533	08:07:01.44	-29:57:10.8	A	7750±150	5.27±0.32	90.28±9.09	5.78E-25	26	27.53	18.74	1.09
				B	50000±3750	0.06±0.01	18.13±1.81	1.83E-21				
BSS 32	NGC 6939	20:31:54.24	+60:40:22.8	A	8750±125	1.78±0.10	16.77±1.67	4.83E-22	19	14.22	17.05	3.73
				B	45000±2500	0.06±0.01	8.93±0.89	7.68E-25				

the sensitivity of *Swift*/UVOT to unveil hot companions that remain elusive in optical bands.

Our analysis of the 35 BSS targets identifies 15 systems exhibiting ultraviolet excess. For the remaining 20 systems, the observed SEDs are well reproduced by single-component models; their best-fit parameters and corresponding SEDs are presented in Appendix A. These BSSs span a broad range of effective temperatures ( $T_{\text{eff}} \approx 7000\text{--}12,750$  K), with radii of  $R \approx 0.9\text{--}4.5 R_{\odot}$  and luminosities between  $L \approx 2$  and  $195 L_{\odot}$ . Most of the effective temperature values are broadly consistent with those reported for BSSs in similar intermediate-age OCs, typically covering 6500–10,250 K (Vaidya et al. 2022b; Panthi & Vaidya 2024). The higher end of our range ( $T_{\text{eff}} \sim 12,000\text{--}12,750$  K) is also in line with what is ex-

pected for more massive BSSs, as found in younger or less evolved clusters where the MSTO occurs at higher temperatures (Sindhu et al. 2019b; Pandey et al. 2021). Such temperatures can be produced through efficient mass transfer or merger processes, which place these objects above the cluster turn-off on the H-R diagram (Bailyn 1995; Ferraro et al. 2009). The generally low goodness-of-fit values (vgf<sub>b</sub>  $\approx 0.45\text{--}3.42$ ) indicate excellent agreement between the models and the observed photometry. The properties of the confirmed binary systems and their evolutionary implications are discussed in detail in the following section.

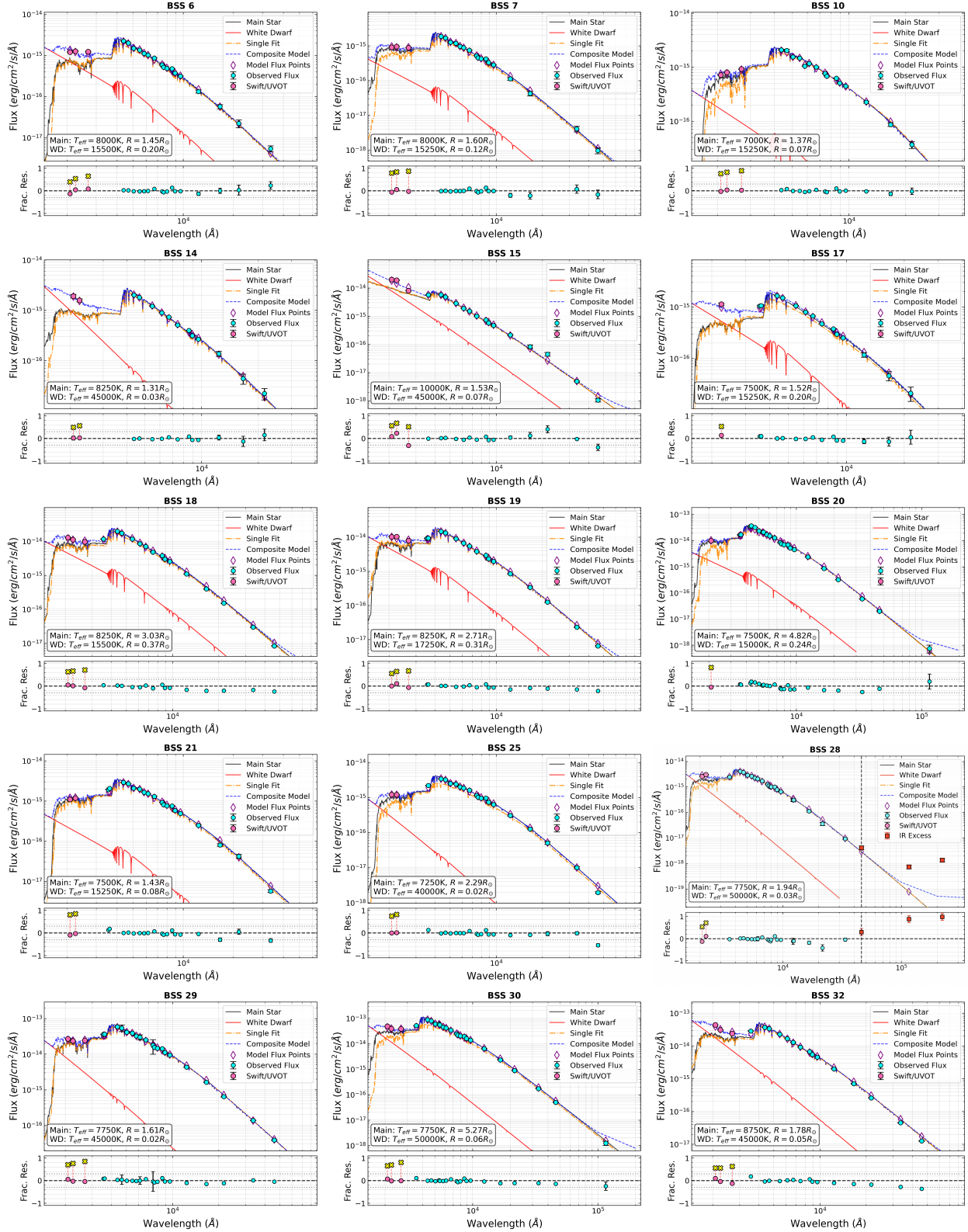


**Figure 5.** Two-component SED fitting analysis for the binary BSS candidates. **Top panels:** Cyan circles with error bars represent the observed multi-wavelength photometric fluxes. The solid black and red curves illustrate the best-fit model spectra of the cool BSS primary (Castelli et al. 1997) and the hot WD secondary (Koester 2010), respectively. The blue-dashed curve shows the total composite model spectrum (primary + secondary). The single-component fit is shown in orange. Purple diamonds denote the synthetic fluxes computed for the corresponding photometric passbands. **Bottom panels:** The fractional residuals between the observed fluxes and the best-fitting composite model. Yellow crosses show the *Swift*/UVOT residuals relative to the single-star Kurucz model of the primary, clearly revealing the UV excess.

#### 4.1. Evolutionary Status of BSSs

The physical properties inferred from the SED fitting offer valuable clues to the evolutionary status of the BSS population. For systems currently consistent with single-component SEDs, the inferred properties suggest that the more luminous objects may correspond to BSSs at relatively advanced evolutionary stages, possibly evolving toward the subgiant branch, as expected from post-MS evolution in this temperature range (e.g., Bressan et al. 2012; Chen et al. 2015; Marigo et al. 2017), whereas the cooler and less luminous targets are compatible with BSSs near the MS turn-off. However, these interpretations should be treated with caution, as the presence of unresolved companions cannot be ruled out. In contrast, the most astrophysically informative results arise from the 15 binary systems identified across seven OCs. The detected hot secondary components are classified into two distinct evolutionary groups based on their temperatures and radii: pre-ELM WDs (stripped-core candidates) and hot WDs.

##### 4.1.1. Pre-ELM WD Candidates

This group comprises a subset of systems in which the hot companions exhibit moderate effective temperatures ( $T_{\text{eff}} \simeq 15,000\text{--}17,250$  K) and relatively large radii ( $R \simeq 0.12\text{--}0.37 R_{\odot}$ ). Such radii are substantially larger than those expected for hot WDs ( $R \sim 0.01 R_{\odot}$ ) and instead are consistent with the predicted properties of proto-WDs or pre-ELM WDs. These objects are interpreted as stripped stellar cores that are still undergoing gravitational contraction and have not yet entered the final WD cooling sequence. In total, six systems in our sample fall into this category (BSS 06, 07, 17, 18, 19, and 20), located in four OCs: Berkeley 31, Berkeley 75, NGC 2192, and NGC 2204 (see Table 6).

To assess their evolutionary status, we placed these companions on the Hertzsprung-Russell (H-R) diagram together with low-mass helium-core evolutionary tracks from Istrate et al. (2016) computed for solar metallicity, and shown in Figure 6. A complementary compilation of previously studied hot component stars, used as a comparison sample in the H-R diagram analysis, is provided in Appendix B. Most of the objects lie close to tracks corresponding to masses of approximately  $M \sim 0.21\text{--}0.26 M_{\odot}$ , consistent with He-core WD evolutionary models (Althaus et al. 2013). Their locations coincide with the pre-ELM contraction phase (thick gray segments in Figure 6), indicating that these objects have not yet reached the temperatures associated with CNO-driven hydrogen-shell flashes nor settled onto the final WD cooling sequence. This strongly suggests that the companions are stripped stellar cores currently under-

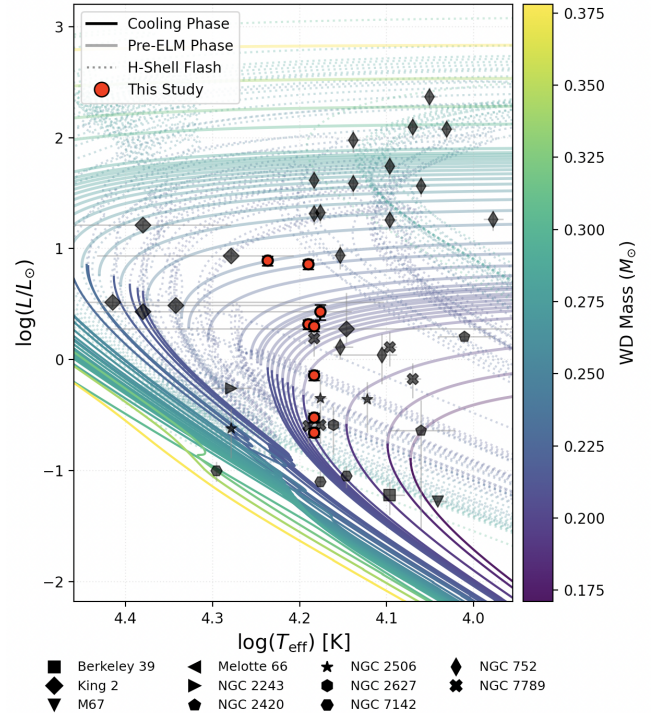


**Figure 6.** The  $\log(L/L_{\odot})$  versus  $\log(T_{\text{eff}})$  diagram showing the evolutionary status of the pre-ELM candidates derived from SED analysis. Red circles indicate the candidates from this study, labeled with the last six digits of their Gaia DR3 IDs. Triangles represent comparison objects from various OCs found in the literature. Theoretical evolutionary tracks are taken from Istrate et al. (2016). The tracks are color-coded by stellar mass and segmented into different evolutionary phases: pre-ELM phase (dashed lines), H-shell flash episodes (dotted lines), and the final cooling phase (solid lines).

going gravitational contraction following recent mass-transfer events (Istrate et al. 2016).

Following the methodology of Dattatreya et al. (2023), we interpolated the evolutionary tracks of Istrate et al. (2016) to assess the evolutionary status of the stripped-core candidates. The reference point is the maximum radius, corresponding to the onset of the pre-ELM contraction phase. Within this framework, most systems occupy similar positions along the contraction sequence, indicating that they are in comparable pre-ELM evolutionary stages (Maxted et al. 2013; El-Badry et al. 2021). Two systems (BSS 10 and BSS 21) are found beyond this phase, lying on the early WD cooling track. In this sense, they can be interpreted as slightly more evolved counterparts of the pre-ELM objects, representing the immediate post-pre-ELM stage within the same evolutionary sequence, rather than a distinct companion class. The relatively large radius inferred for BSS 18 ( $0.37 R_{\odot}$ ) remains consistent with the expected range

( $\sim 0.1\text{--}0.6 R_{\odot}$ ) for proto-ELM objects during the early contraction phase (Istrate et al. 2016).

The host OCs in our sample span a broad range of intermediate ages, extending from a few hundred Myr to nearly 2 Gyr. At these ages, the corresponding MSTO masses are typically of order  $\sim 2\text{--}2.5 M_{\odot}$ , significantly higher than those characteristic of old GCs. This implies that the progenitors of the identified pre-ELM candidates were intermediate-mass stars. Consequently, our results indicate that in intermediate-age OC environments, binary evolution involving relatively massive progenitors can lead to the formation of low-mass helium-core pre-WD dwarfs. These evolutionary pathways are likely distinct from those commonly inferred in GC populations, where the progenitor masses are substantially lower.

#### 4.1.2. Hot WD Candidates

In contrast to the pre-ELM or stripped-core candidates, a distinct subset of systems in our sample hosts extremely hot and compact companions that are fully consistent with canonical WDs. These objects are characterized by very high effective temperatures ( $T_{\text{eff}} \gtrsim 40,000$  K and reaching up to  $\sim 80,000$  K) and small radii ( $R \sim 0.02\text{--}0.03 R_{\odot}$ ), with surface gravities omitted since they cannot be robustly constrained from SED analysis. Such parameters place them firmly on the WD cooling sequence and clearly separate them from the pre-ELM population discussed above.

The adopted radius range for the hot WD companions is consistent with theoretical mass-radius relations for carbon-oxygen (CO) and oxygen-neon (ONe) core WDs in the mass range  $0.4 \lesssim M/M_{\odot} \lesssim 1.3$  (Nauenberg 1972; Althaus et al. 2010). At these masses, degenerate equation-of-state models predict radii of approximately  $0.008\text{--}0.018 R_{\odot}$  for the most massive WDs and up to  $\sim 0.04 R_{\odot}$  for lower-mass CO-core remnants (Koester 2010). The inferred radii in our sample fall within this theoretically expected range and are furthermore consistent with values reported for hot WD companions in similar SED-based studies of OC BSSs (e.g., Pandey et al. 2021; Rao et al. 2022b; Vaidya et al. 2022a; Sheikh & Medhi 2024b; Bisht et al. 2026a).

Seven systems in our sample fall into this category (BSS 14, 15, 25, 28, 29, 30, and 32; see Table 6). The hottest companions identified in our sample reach effective temperatures of  $T_{\text{eff}} \approx 50,000$  K. These properties are broadly consistent with theoretical mass-radius relations for hot WDs (e.g., Althaus et al. 2010; Koester 2010), indicating fully degenerate remnants formed after core helium ignition in the progenitor.

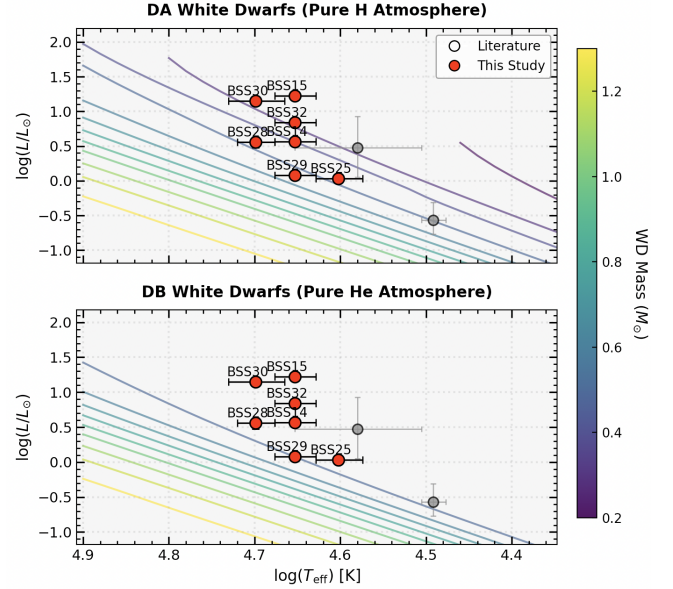


**Figure 7.** Comparison of theoretical cooling tracks with the observational positions of the WD candidates in the H-R diagram. The upper and lower panels show models for DA and DB WDs, respectively. The solid colored curves represent evolutionary cooling tracks for WDs with masses in the range  $0.2 \leq M/M_{\odot} \leq 1.3$ . The color of each track corresponds to the WD mass, as indicated by the color bar on the right. The evolutionary models are adopted from Camisassa (2025). Red circles mark the hot WD candidates analyzed in this work, while gray circles show comparison systems from the literature in Melotte 66 and NGC 6940. Error bars indicate the uncertainties in the derived effective temperature and luminosity.

The detection of such hot and compact remnants provides strong evidence for a post-mass-transfer evolutionary origin. Given their extreme temperatures, these WDs are expected to be very young objects on the cooling sequence, with cooling ages of at most a few Myr according to modern WD evolutionary models (Bédard et al. 2020). This implies that mass transfer in these systems must have ceased very recently on evolutionary timescales, and that the companions have only just settled onto the WD cooling track following envelope ejection, possibly via a common-envelope phase.

Unlike the pre-ELM candidates, which represent stars that have undergone interrupted stellar evolution before core helium ignition, these hot, luminous companions follow the standard cooling sequences of fully evolved WDs. By interpolating their positions across the recent DA (pure hydrogen atmosphere) and DB (pure helium atmosphere) model grids (e.g., Camisassa 2025), we systematically derived their current masses, cooling ages, and corresponding progenitor masses. Their presence in blue straggler systems underscores the remarkable di-

versity of mass-transfer pathways operating in OCs, producing a wide spectrum of stellar remnants that ranges from stripped, low-mass helium cores to massive CO and ONe WDs.

#### 4.2. Dynamical State of Host Clusters and Implications for BSS Formation

The presence and distribution of BSSs within clusters provide important insights into their dynamical evolution. In low-density OCs, stellar collisions are expected to be rare, and binary evolution is the dominant mechanism responsible for BSS formation (Mathieu & Geller 2009; Leigh et al. 2011). The identification of numerous BSS systems hosting hot degenerate companions in our sample strongly supports this scenario. The ages of the studied clusters range from approximately 0.7 to 2 Gyr, corresponding to MSTO masses of  $\sim 1.5\text{--}2.5 M_{\odot}$ . At these ages, binary mass transfer involving intermediate-mass progenitors is expected to efficiently produce BSSs and low-mass WD companions. The presence of both pre-ELM and fully formed WDs in our sample indicates that binary evolution is ongoing and spans multiple evolutionary stages.

##### 4.2.1. Radial Distribution and Mass Segregation

We analyzed the radial distributions of the BSS candidates relative to other cluster members to assess their dynamical states. Because BSSs are generally more massive than mean cluster members, they are expected to undergo mass segregation and migrate toward the cluster core via dynamical friction over time. We calculated the projected distance of each star from the cluster center using Gaia DR3 coordinates (Gaia Collaboration et al. 2023). For comparison, cluster members were divided into two reference populations using a cluster-specific magnitude limit ( $G_{\text{lim}}$ ) to separate evolved turn-off and giant stars from the lower MS.

Figure 8 shows the resulting radial cumulative distribution functions (RCDFs), comparing BSS candidates to the bright ( $G \leq G_{\text{lim}}$ ) and faint ( $G > G_{\text{lim}}$ ) reference populations. We performed a two-sample Kolmogorov-Smirnov (KS) test to compare the radial distributions of the BSS candidates and the unsegregated faint population. The resulting  $p$ -values ( $p_{\text{KS}}$ ) quantify the probability that both samples are drawn from the same parent distribution;  $p_{\text{KS}} < 0.05$  indicates statistically significant mass segregation.

The RCDFs reflect the expected mass hierarchy within the clusters. Evolved stars (giants; orange dashed lines) are more centrally concentrated than the lower-mass MS stars (dwarfs; red solid lines), which dominate the cluster outskirts (typically at  $r > 10$  pc). The BSS and evolved RCDFs rise steeply and reach unity at

smaller radii, demonstrating spatial stratification and confirming mass segregation among the more massive stellar populations.

In clusters such as NGC 2204 and NGC 6939, BSS candidates exhibit a strong central concentration relative to the faint population ( $p_{\text{KS}} = 0.016$  and  $0.006$ , respectively). This indicates that these clusters are dynamically relaxed and their BSS populations are mass-segregated (Ferraro et al. 2012). In OCs with few BSSs (e.g., Berkeley 29,  $N = 1$ ), statistical significance is inherently limited, though the candidates still preferentially reside in the inner regions. Overall, the BSS spatial distributions closely track those of the massive, bright members (Lanzoni et al. 2016).

In the low-density environments of OCs, BSS formation is primarily driven by mass transfer in binary systems, where the progenitor accretes mass from a donor that later evolves into a WD (Geller & Mathieu 2011). Our identification of BSS candidates with degenerate companions at various evolutionary stages (pre-ELM, cooling, and hot WDs; see Table 6) supports this channel.

The dynamical analysis highlights varying degrees of mass segregation among these binary systems. The highly segregated BSS population in NGC 6939 is consistent with massive binaries (BSS+WD) that have migrated to the core, aligning with the detection of a  $\sim 0.6 M_{\odot}$  hot WD companion. NGC 2204 similarly shows clear segregation and hosts diverse companions. Conversely, the radial distributions of BSSs in NGC 2533 ( $p_{\text{KS}} = 0.996$ ) and NGC 2192 ( $p_{\text{KS}} = 0.446$ ) are statistically indistinguishable from the reference populations. This lack of segregation may reflect a younger dynamical age or a less dynamically evolved cluster environment. However, the presence of pre-ELM companions (e.g., BSSs 18 and 19 in NGC 2192) indicates that the mass-transfer mechanism operates actively even before significant dynamical relaxation occurs (Gosnell et al. 2015; Bisht et al. 2026b).

To provide a more quantitative dynamical context for the KS test results, we estimated the relaxation time  $t_{\text{relax}}$  for each cluster following the standard approximation (Binney & Tremaine 2008):

$$t_{\text{relax}} = \frac{0.138 N^{1/2} R_{\text{h}}^{3/2}}{G^{1/2} \bar{m}^{1/2} \ln(0.4 N)}, \quad (3)$$

where  $N$  is the number of cluster members,  $R_{\text{h}}$  is the half-mass radius,  $\bar{m}$  is the mean stellar mass, and  $G$  is the gravitational constant. The member counts, total masses, mean masses, and half-mass radii were adopted from the catalog of Hunt & Reffert (2024). The ratio  $t_{\text{age}}/t_{\text{relax}}$  provides an estimate of how many relaxation

**Table 6.** Properties of BSS systems with masses and radii estimated from evolutionary-track interpolation. The cool component corresponds to the BSS, while the hot component represents the WD companion. For hot WD systems, values are given as H/He. Missing values are indicated with ‘-’.

BSS ID	Evolutionary Stage	Cool Component (A)		Hot Component (B)	
		Mass ( $M_{\odot}$ )	Radius ( $R_{\odot}$ )	Mass ( $M_{\odot}$ )	Radius ( $R_{\odot}$ )
BSS 06	1	1.35±0.02	1.45±0.09	0.263±0.002	0.20±0.01
BSS 07	1	1.36±0.03	1.60±0.10	0.260±0.008	0.12±0.01
BSS 10	2	1.17±0.04	1.37±0.10	0.256±0.030	0.07±0.01
BSS 14	3	1.37±0.03	1.31±0.10	0.399±0.067/-	0.03±0.01/-
BSS 15	3	1.51±0.01	1.53±0.08	0.258±0.012/-	0.07±0.01/-
BSS 17	1	1.28±0.03	1.52±0.10	0.210±0.001	0.20±0.01
BSS 18	1	1.85±0.02	3.04±0.21	0.228±0.003	0.37±0.02
BSS 19	1	1.83±0.02	2.71±0.18	0.233±0.001	0.31±0.02
BSS 20	1	1.53±0.00	4.84±0.41	0.213±0.003	0.24±0.02
BSS 21	2	1.27±0.03	1.44±0.09	0.216±0.008	0.08±0.01
BSS 25	3	1.52±0.01	2.29±0.15	0.474±0.044/0.500±0.010	0.02±0.01/0.02±0.01
BSS 28	3	1.45±0.03	1.95±0.19	0.469±0.041/-	0.02±0.01/-
BSS 29	3	1.32±0.03	1.61±0.11	0.543±0.053/0.500±0.049	0.02±0.01/0.02±0.01
BSS 30	3	2.14±0.03	5.28±0.33	0.288±0.038/-	0.05±0.01/-
BSS 32	3	1.60±0.06	1.78±0.10	0.292±0.035/-	0.04±0.01/-

(1) pre-ELM, (2) cooling, (3) hot WD.

times a cluster has undergone since formation, and thus how dynamically evolved it is expected to be. Among our nine clusters, NGC 2204 and NGC 6939 stand out with the highest  $t_{\text{age}}/t_{\text{relax}}$  ratios, and these are precisely the two clusters that show statistically significant mass segregation in the KS test ( $p_{\text{KS}} = 0.016$  and  $0.006$ , respectively). This correspondence is broadly consistent with the expectation that more dynamically evolved clusters have had more time to redistribute their more massive members toward the core through dynamical friction (Ferraro et al. 2012; Lanzoni et al. 2016).

In contrast, clusters such as NGC 2533 and NGC 2192 show no statistically significant segregation ( $p_{\text{KS}} = 0.996$  and  $0.446$ , respectively), despite having non-negligible relaxation timescales. This suggests that either the clusters have not yet completed enough relaxation cycles or that the small number of BSSs in these systems limits the statistical power of the KS test. We caution that the connection between  $t_{\text{relax}}$  and BSS segregation is not one-to-one in our sample; other factors, such as cluster richness, the initial binary fraction, and the mass of the BSS systems, likely also play a role. These results should therefore be interpreted as broadly indicative rather than definitive.

#### 4.3. Binary Fraction of Host Clusters

To provide a simple comparison with our UV-excess BSS results, we estimated the photometric binary fraction for each of the nine clusters. We followed the CMD-based approach of Milone et al. (2012), also used by Donada et al. (2023). MS members were selected from the catalogues of Hunt & Reffert (2024). The resulting  $t_{\text{relax}}$

values are listed in Table 4. For each cluster, we defined a single-star sequence by fitting a fourth-degree polynomial to the median color–magnitude relation. Stars lying more than 0.75 mag above this sequence were considered binary candidates (roughly  $q \gtrsim 0.6$ ). The binary fraction was then computed as:

$$f_{\text{b}} = \frac{N_{\text{bin}}}{N_{\text{MS}}}, \quad (4)$$

where  $N_{\text{bin}}$  is the number of binary candidates and  $N_{\text{MS}}$  is the number of main-sequence stars. Uncertainties were estimated using 95% Wilson confidence intervals. The resulting values listed in Table 7 range from  $f_{\text{b}} \approx 0.04$  to 0.15. These are generally on the lower side compared to the broader sample of Donada et al. (2023), which is expected since our estimates mainly trace binaries with relatively high mass ratios. Within our sample, NGC 6939, NGC 2533, and NGC 2204 show the highest fractions, while Berkeley 29 and Berkeley 37 have the lowest.

Table 7 shows a weak indication that clusters with higher binary fractions may host more binary BSS systems, although the trend is not clear. For example, Berkeley 31 and NGC 2204, which have the largest BSS populations in our sample, also contain the highest numbers of UV-excess systems. On the other hand, Berkeley 75 and NGC 2192 show relatively high fractions of binary BSSs among their small BSS samples, consistent with the expectations that binary-rich environments can favour BSS formation via mass transfer (Mathieu & Geller 2009; Knigge et al. 2009).

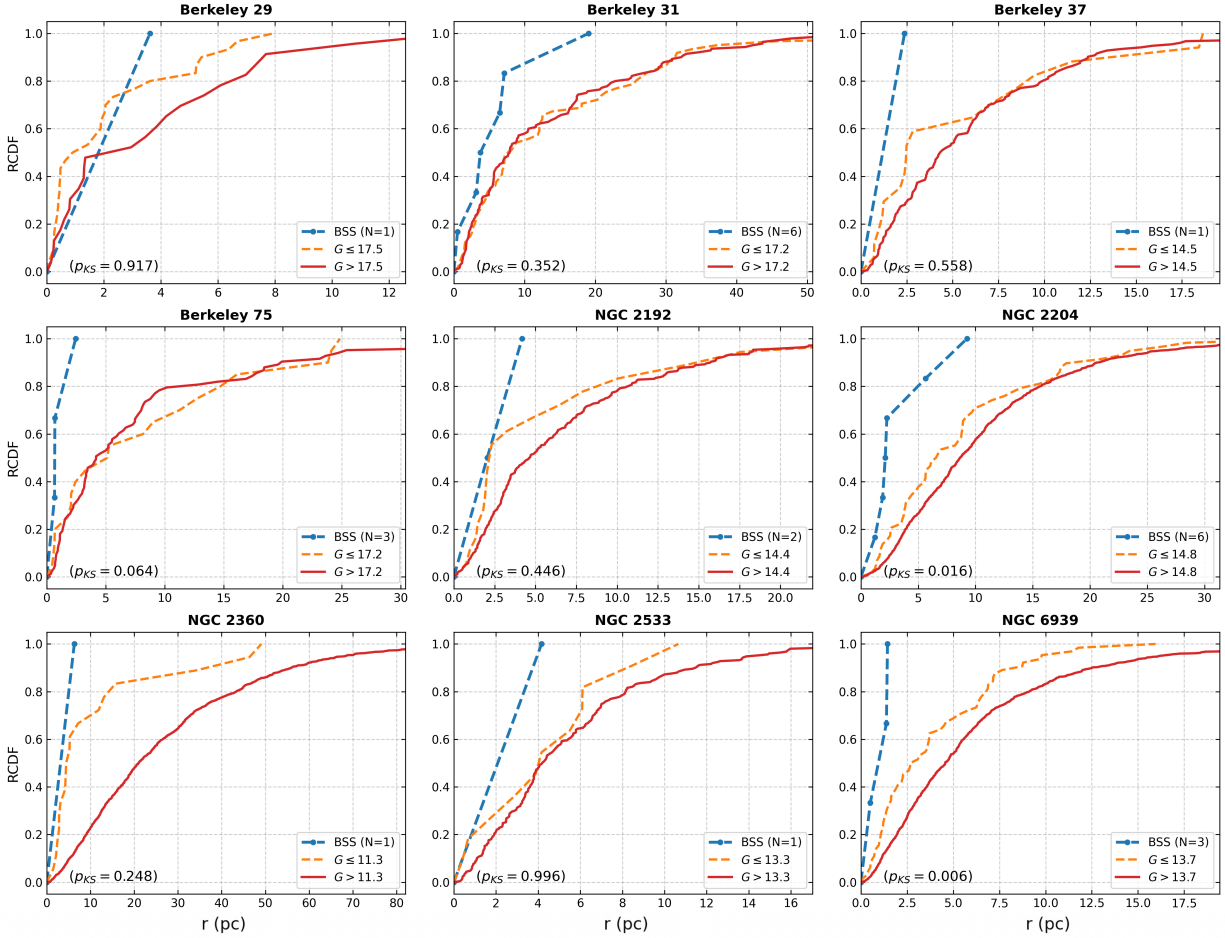


**Figure 8.** RCDFs of BSSs (blue dashed lines), evolved stars (orange dashed lines), and MS stars (red solid lines) for each cluster. The projected distance from the cluster center is shown on the horizontal axis. The MS and evolved samples are defined relative to the MSTO lines indicated in the corresponding CMDs. The number of BSSs in each cluster is indicated in the legend. The KS test probabilities ( $p_{KS}$ ) comparing the radial distributions of BSSs and the reference populations are reported in each panel.

NGC 6939, despite having the highest binary fraction, contains only one UV-excess BSS out of five. This may be related to its more advanced dynamical state (Section 4.2.1), where the KS test ( $p_{KS} = 0.006$ ) indicates strong mass segregation. In such dynamically evolved clusters, massive systems are expected to concentrate toward the core, where crowding can make UV detections more difficult or where past interactions may have altered some binaries (Leigh et al. 2011; Ferraro et al. 2012). Overall, these patterns should be interpreted with caution. The number of binary BSSs per cluster is small, and our photometric binary fractions mainly trace systems with  $q \gtrsim 0.6$  (Donada et al. 2023). A larger and more homogeneous sample would be needed to clarify whether a real connection exists (Childs & Geller 2025; Mikhnevich et al. 2026; Malhotra et al. 2026).

**Table 7.** Photometric binary fractions estimated from the Gaia CMD for the nine host clusters.  $N_{BSS}$  is the total number of BSSs,  $N_{BSS,bin}$  is the number of UV-excess binary BSS systems, and the uncertainties represent 95% Wilson binomial confidence intervals.

Cluster	$N_{BSS}$	$f_b$	$N_{BSS,bin}$
Berkeley 31	6	$0.09^{+0.06}_{-0.04}$	3
Berkeley 29	1	$0.04^{+0.17}_{-0.04}$	-
Berkeley 37	1	$0.04^{+0.05}_{-0.02}$	-
Berkeley 75	3	$0.08^{+0.08}_{-0.04}$	3
NGC 2192	2	$0.08^{+0.06}_{-0.04}$	2
NGC 2204	6	$0.12^{+0.03}_{-0.03}$	4
NGC 2360	1	$0.06^{+0.03}_{-0.02}$	1
NGC 2533	1	$0.12^{+0.06}_{-0.04}$	1
NGC 6939	3	$0.15^{+0.03}_{-0.03}$	1

#### 4.4. Dynamical Environment of the Clusters

To investigate the dynamical environments of the clusters hosting BSSs with compact companions, we computed the Galactic orbits of the clusters in our sample. The orbital calculations were performed using six-dimensional (6D) phase-space information derived from Gaia DR3 astrometry, including positions, trigonometric parallaxes, proper motion components, and available radial velocities. The orbit integrations were carried out with the `galpy` Python package (Bovy 2015), adopting the `MWPotential2014` Galactic potential model for the Milky Way, which consists of a Miyamoto-Nagai disk (Miyamoto & Nagai 1975), a Hernquist bulge (Hernquist 1990), and a logarithmic halo (Binney & Tremaine 2008). A Galactocentric distance of  $R_{gc} = 8$  kpc, a circular rotation speed of  $V_{rot} = 220$  km s $^{-1}$  (Bovy & Tremaine 2012; Bovy 2015), and a vertical distance of the Sun from the Galactic plane of  $27 \pm 4$  pc (Chen et al. 2000) were adopted. The integrations were performed over timescales corresponding to the cluster ages listed in Table 4, which were adopted from Hunt & Reffert (2024). An example of the resulting orbital trajectory, corresponding to Berkeley 31, is presented in Figure 9. The figure shows the cluster’s motion both within the Galactic plane ( $X_{Gal}$ – $Y_{Gal}$ ) and in the vertical direction ( $X_{Gal}$ – $Z_{Gal}$ ) (see also, Tanık Öztürk et al. 2025; Karagöz et al. 2025; Taşdemir et al. 2026).

Because the number of clusters hosting BSSs with confirmed WD companions in our study is limited, we expanded the sample by compiling additional systems from the literature where WD companions to BSSs have been reported. In total, 14 OCs (see Table 1) from previous studies were added to our sample, resulting in a combined dataset of 23 OCs. This expanded sample allows us to explore statistical relationships between cluster structural parameters and the BSS population.

To characterize the spatial distribution of BSSs within each cluster, we calculated the  $r_{50}$  parameter for the BSS population. For each BSS, the projected distance from the cluster center was determined, and the radius containing half of the BSS population was adopted as  $r_{50}$ . The use of  $r_{50}$  provides a robust statistical description of the typical radial location of BSSs while minimizing the effects of small-number statistics. Unlike structural parameters such as the core or half-mass radius, which depend on global cluster properties and model assumptions,  $r_{50}$  directly reflects the observed spatial distribution of the BSS population itself. This makes it a convenient and consistent parameter for comparing BSS distributions across clusters with different sizes and structural characteristics.

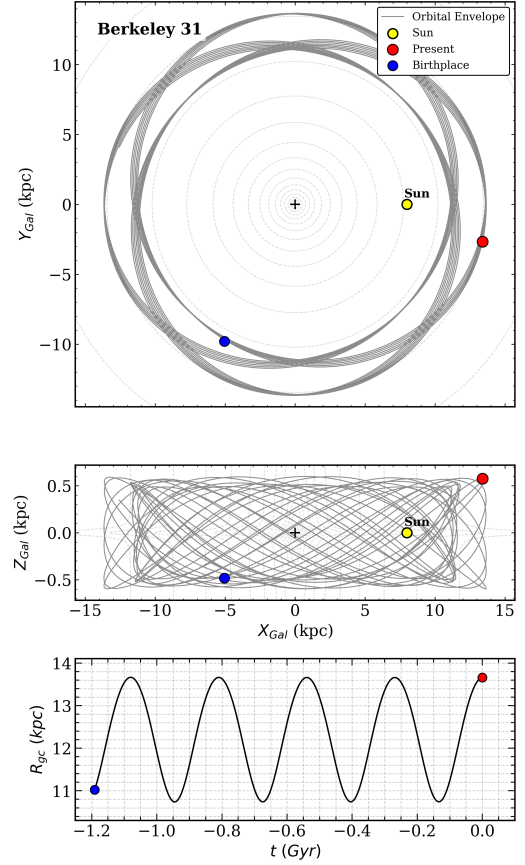


**Figure 9.** Galactic orbital paths for Berkeley 31. The top panel shows the orbital projection on the Galactic  $X - Y$  plane, while the middle panel illustrates the motion perpendicular to the plane ( $X - Z$ ). In both panels, the gray curves represent the integrated orbital envelope, and a yellow circle indicates the Sun. The cluster’s current position and birthplace are marked with red and blue circles, respectively. The bottom panel displays the evolution of the Galactocentric distance ( $R_{gc}$ ) as a function of look-back time ( $t$ ), where the black solid line traces the trajectory since formation. In this panel, the yellow circle represents the present-day distance, and the orange inverted triangle marks the birth distance. The grey dashed contours represent the logarithmic mass density of the Milky Way as described by the `MWPotential2014` model.

To place these measurements in a Galactic dynamical context, we compared the derived  $r_{50}$  values with the early orbital radius parameter ( $R_{teo}$ ). The  $R_{teo}$  parameter represents the approximate early orbital configuration of a stellar system. It is calculated by tracing its orbit backward in time using the present-day phase-space coordinates and cluster age (Bovy 2015). In this approach, orbital integration is performed under the assumption of a static Galactic potential, and numerous studies in the literature address this assumption (e.g., Taşdemir & Yontan 2023; Yontan & Canbay

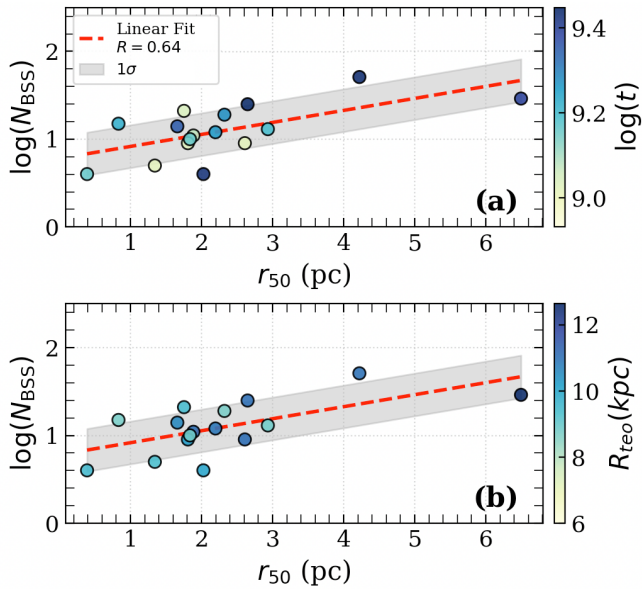


**Figure 10.** Correlation between the half-light radius  $r_{50}$  and the number of BSSs ( $\log N_{\text{BSS}}$ ) in OCs. Color coding represents cluster age ( $\log t$ ) in panel (a) and theoretical birth radius ( $R_{\text{teo}}$ ) in panel (b). The dashed red line indicates the linear fit, while the shaded gray area denotes the  $1\sigma$ .

2023; Yücel et al. 2024; Çınar et al. 2024; Taşdemir et al. 2025). While  $R_{\text{teo}}$  does not represent the exact birth radius of a cluster, it provides an estimate of its early orbital characteristics without relying on assumptions about the metallicity gradient of the Galactic disk. The  $R_{\text{teo}}$  values used in this work were obtained using the methodology described in Minchev et al. (2013). Cluster ages were adopted from Hunt & Reffert (2024), thereby allowing us to trace the clusters’ orbital evolution back to their early dynamical configurations.

Figure 10 shows the relationship between the half-number radius of BSSs ( $r_{50}$ ) and the logarithm of the number of BSSs ( $\log N_{\text{BSS}}$ ) for the cluster sample. Panel (a) shows the distribution color-coded by cluster age, while panel (b) displays the same relation color-coded by the early orbital radius  $R_{\text{teo}}$ . A positive correlation between  $r_{50}$  and  $\log N_{\text{BSS}}$  is visible, with the linear fit yielding  $\log N = 0.14 \times r_{50} + 0.78$  and a moderate correlation coefficient ( $R = 0.64$ ).

This trend suggests that clusters with larger characteristic BSS radii tend to host larger BSS populations. Such behavior may reflect the influence of cluster structural properties and dynamical evolution on the formation and survival of BSS systems. Older clusters or those with larger orbital radii in the Galactic disk tend to occupy relatively quiescent dynamical environments, where tidal perturbations are weaker (e.g., Carraro et al. 2007, 2013; Angelo et al. 2020, 2023; Bilir et al. 2026).

At the same time, it should be noted that cluster survival is mass-dependent: more massive clusters are generally more likely to persist to older ages, while lower-mass clusters are more easily disrupted. Therefore, the larger number of BSSs (and larger orbital radii) observed in older clusters may partly reflect this selection effect, in addition to the influence of weaker tidal perturbations. These conditions can allow primordial binaries to survive for long timescales and evolve through mass transfer, producing BSS+WD systems.

Although the sample size remains limited, the observed trend hints that both the internal structure of clusters and their Galactic dynamical history may influence the observed BSS population. All calculated parameters, including the literature clusters and the derived  $r_{50}$  and  $R_{\text{teo}}$  values, were included in the final analysis.

## 5. SUMMARY AND CONCLUSION

In this study, we have conducted a systematic multi-wavelength characterization of 35 candidate stars distributed across nine OCs. By anchoring our dataset with high-sensitivity NUV photometry from *Swift*/UVOT and complementing it with optical-to-IR data from Gaia DR3, Pan-STARRS, and 2MASS/WISE, we constructed robust SEDs to probe for the presence of hot, subluminal companions. We further contextualized these photometric findings by reconstructing the Galactic orbits of the host clusters, thereby linking the internal binary evolution of the BSSs to their external dynamical environments.

The main findings are summarized as follows:

- Our SED analysis revealed that 20 systems are consistent with single-component atmosphere models or possess companions that remain unresolved at UV wavelengths. In contrast, 15 BSSs exhibited significant UV excesses requiring two-component SED fits, providing evidence for hot, compact companions and a binary origin (Gosnell et al. 2015; Vaidya et al. 2022b; Chand et al. 2024b).
- Among the binary systems, our analysis suggests the presence of hot companions likely representing distinct post-mass-transfer stages, specifically young, hot WDs and pre-ELM WD candidates. The coexistence of these binary systems alongside single-fit BSSs points to the heterogeneous nature of the BSS population in intermediate-age OCs, supporting the scenario that mass transfer is a major formation pathway, consistent with previous studies (e.g., Subramaniam et al. 2016; Vaidya

- et al. 2024). Component masses derived from evolutionary-track interpolation suggest BSS primaries in the range  $\sim 1.2\text{--}2.1 M_{\odot}$  and WD companions spanning  $\sim 0.21\text{--}0.54 M_{\odot}$ , consistent with intermediate-mass binary progenitors undergoing mass transfer in OC environments.
- Radial spatial distributions confirmed that the identified BSS candidates predominantly inhabit the central regions of their host clusters, which is a direct signature of mass segregation driven by dynamical friction. Distinct segregation within clusters such as NGC 6939 indicates a dynamically relaxed state. Conversely, a lack of strong segregation in clusters such as NGC 2192 and NGC 2360 suggests these environments may be dynamically younger or that their BSS populations formed too recently to have migrated inward.
  - We estimated the photometric binary fractions for the nine host clusters using a CMD-based method (Milone et al. 2012). The derived values range from  $f_b \approx 0.04$  to 0.15, with NGC 6939, NGC 2533, and NGC 2204 having the highest fractions. There is a tentative indication that clusters with higher binary fractions may host more UV-excess BSS systems; however, this trend is not statistically robust due to the limited sample size. For example, NGC 6939 contains only one UV-excess BSS, possibly due to its advanced dynamical state and observational limitations in crowded regions. A larger and more homogeneous sample is needed to test this relation more reliably (Childs & Geller 2025; Mikhnevich et al. 2026; Malhotra et al. 2026).
  - Orbital solutions derived from Gaia DR3 astrometry show that clusters hosting BSSs with hot companions follow stable, mildly eccentric orbits confined to the Galactic disk. This kinematic configuration is typical for OCs and implies that they evolve in relatively quiescent dynamical environments, co-rotating with the disk and experiencing only weak tidal perturbations. As a result, these systems are largely shielded from strong tidal shocks or disruptive encounters with giant molecular clouds (Spitzer 1987; Gieles et al. 2006; Kruijssen 2012). This suggests that dynamical stellar collisions are unlikely to play a significant role, and that the observed BSS systems are more consistently explained by long-term binary evolution through stable mass transfer (Mathieu & Geller 2015).
  - Our analysis reveals a positive correlation ( $R = 0.64$ ) between the half-number radius of the BSS population ( $r_{50}$ ) and the logarithm of the number of BSSs ( $\log N_{\text{BSS}}$ ). When examined alongside cluster age and early orbital radius ( $R_{\text{teo}}$ ), this trend suggests that clusters with larger characteristic BSS radii tend to host larger BSS populations.

The detection of both hot WDs and pre-ELM candidates highlights the diverse range of interaction products present in OCs. Future spectroscopic follow-up is strongly encouraged to determine radial velocities, orbital periods, and mass ratios for these systems, thereby providing definitive constraints on binary evolution models.

#### ACKNOWLEDGMENTS

We sincerely thank the anonymous referee for a thorough review and constructive suggestions that greatly improved the clarity and quality of the manuscript. This study is a part of the PhD Thesis of Deniz Cennet Çınar. This work uses data from the European Space Agency’s Gaia mission, processed by the Gaia Data Processing and Analysis Consortium (DPAC). Ultraviolet data were obtained from the Neil Gehrels Swift Observatory using calibrated Level-3 UVOT point-source catalogs. Optical photometry was taken from Pan-STARRS1 and the SkyMapper Southern Survey. Near- and mid-infrared data were obtained from 2MASS and WISE. NASA’s Astrophysics Data System, as well as the VizieR and SIMBAD databases operated by CDS in Strasbourg, France, were used. This work has also used data from the European Space Agency (ESA) mission Gaia (<https://www.cosmos.esa.int/gaia>), processed by the Gaia Data Processing and Analysis Consortium (DPAC; <https://www.cosmos.esa.int/web/gaia/dpac/consortium>). Funding for the DPAC is provided by national institutions, in particular those participating in the Gaia Multilateral Agreement. This publication makes use of VOSA, developed under the Spanish Virtual Observatory (<https://svo.cab.inta-csic.es>) project funded by MCIN/AEI/10.13039/501100011033/ through grant PID2020-112949GB-I00. VOSA has been partially updated with funding from the European Union’s Horizon 2020 Research and Innovation Programme under Grant Agreement No. 776403 (EXOPLANETS-A).

*Facilities:* Swift(UVOT), Gaia, Pan-STARRS, SkyMapper, 2MASS, WISE

**Table 8.** Results of the single SED fitting analysis, showing the derived parameters for the BSS candidates. The columns list the host cluster, *Gaia* DR3 source identifier, and equatorial coordinates ( $\alpha$ ,  $\delta$ ). For each target star, the derived fundamental parameters are provided: effective temperature ( $T_{\text{eff}}$ ), radius ( $R$ ), and luminosity ( $L$ ). Finally, the scaling factors, the number of photometric points used in the fit ( $N_{\text{fit}}$ ), reduced chi-square ( $\chi^2_{\nu}$ ), and the goodness-of-fit metric (vgf and vgf<sub>b</sub>) are presented.

No	Cluster	$\alpha$ (hh:mm:ss)	$\delta$ (dd:mm:ss)	$T_{\text{eff}}$ (K)	$R$ ( $R_{\odot}$ )	$L$ ( $L_{\odot}$ )	Scaling Factor	$N_{\text{fit}}$	$\chi^2_{\nu}$	vgf	vgf <sub>b</sub>
BSS 01	Berkeley 29	06:53:13.59	+16:55:24.26	7500±172	0.98±0.05	2.81±0.50	1.57E-23	11	162.25	41.49	1.67
BSS 02	Berkeley 31	06:57:17.42	+08:18:24.37	10000±274	2.20±0.11	44.04±8.78	2.16E-22	25	11.19	7.15	1.48
BSS 03	Berkeley 31	06:57:36.93	+08:15:25.49	8000±167	1.25±0.06	5.74±1.10	3.39E-23	13	169.71	29.05	0.56
BSS 04	Berkeley 31	06:57:43.62	+08:16:51.60	10000±301	1.14±0.06	11.80±1.89	2.93E-23	20	4.94	4.88	0.93
BSS 05	Berkeley 31	06:57:36.17	+08:16:29.10	8000±174	1.50±0.07	8.35±1.25	9.08E-23	15	36.04	14.16	0.62
BSS 08	Berkeley 31	06:57:48.73	+08:16:02.50	7500±125	1.54±0.08	6.70±0.70	7.84E-23	18	22.48	7.99	2.31
BSS 09	Berkeley 31	06:57:38.82	+08:16:26.62	7500±212	0.93±0.05	2.48±0.47	2.40E-23	14	2.53	2.52	0.45
BSS 11	Berkeley 31	06:57:39.96	+08:18:13.68	8000±125	2.57±0.13	23.92±2.40	7.77E-23	24	44.96	7.15	2.26
BSS 12	Berkeley 31	06:57:33.78	+08:18:12.09	7500±159	1.35±0.06	5.18±0.81	4.56E-23	15	76.70	12.38	0.51
BSS 13	Berkeley 37	07:20:16.87	-01:01:29.51	12250±125	2.58±0.13	138.26±14.43	1.70E-22	19	365.99	22.12	1.04
BSS 16	Berkeley 75	06:48:52.55	-23:59:09.63	7250±125	1.12±0.06	3.14±0.32	2.01E-23	19	385.61	11.61	0.53
BSS 22	NGC 2204	06:15:39.17	-18:40:04.98	8000±173	3.32±0.17	40.62±6.84	1.30E-22	20	53.42	6.43	1.69
BSS 23	NGC 2204	06:15:35.42	-18:39:50.76	11000±164	3.29±0.16	142.38±19.99	3.06E-22	23	105.08	11.26	0.46
BSS 24	NGC 2204	06:15:47.65	-18:38:10.18	12750±285	1.75±0.08	72.88±11.58	8.64E-23	21	319.73	18.88	0.74
BSS 25	NGC 2204	06:15:31.42	-18:38:51.68	9750±125	2.72±0.14	62.35±6.69	1.60E-22	23	410.58	9.13	1.2
BSS 27	NGC 2204	06:15:36.18	-18:42:19.48	7000±196	2.18±0.11	10.40±1.97	7.85E-23	15	655.64	26.20	1.29
BSS 31	NGC 6939	20:31:31.89	+60:38:15.81	12000±125	3.11±0.16	184.26±21.72	1.50E-21	19	260.49	39.34	2.36
BSS 33	NGC 6939	20:31:31.93	+60:36:25.46	7500±298	4.22±0.21	50.73±11.74	2.56E-21	18	530.73	39.69	1.58
BSS 34	NGC 6939	20:31:31.93	+60:36:25.46	8500±166	3.86±0.19	70.99±10.59	2.34E-21	19	376.99	55.47	3.42
BSS 35	NGC 6939	20:31:31.89	+60:38:15.80	12250±125	3.04±0.15	195.58±22.68	1.45E-21	14	208.46	29.87	1.59

*Software:* VOSA (Bayo et al. 2008), galpy (Bovy 2015), Aladin

## APPENDIX

### A. SINGLE-COMPONENT SED FITS OF STUDIED BSSS

In this appendix, we present the full set of single-component SED fits for the BSS candidates that are well reproduced by single-star atmosphere models. The fitting procedure follows the methodology described in Section 3.2, where observed multi-wavelength fluxes were modeled using Kurucz ODFNEW/NOVER grids (Castelli et al. 1997; Castelli & Kurucz 2003). within the VOSA framework. The derived fundamental stellar parameters for the entire sample, including  $T_{\text{eff}}$ , radius, and luminosity, are listed in Table 8. The corresponding SED fits are shown in Figure 11, where each panel displays the observed photometric data points along with the best-fitting theoretical model.

### B. DATA OF LITERATURE-STUDIED HOT COMPONENT STARS

We compile a homogeneous list of literature-studied hot component stars whose atmospheric and evolutionary parameters have been previously reported. For a subset of objects lacking mass estimates in the literature, we derived approximate masses by placing them on the H-R diagram and comparing their positions with the evolutionary tracks of Istrate et al. (2016), following the same approach adopted for our sample. The full set of compiled parameters is presented in Table 9. These objects are used as a comparison sample in the H-R diagram shown in Figure 6, where they are plotted together with our pre-ELM candidates.

## REFERENCES

- Ahumada, J. A., & Lapasset, E. 2007, A&A, 463, 789, doi: 10.1051/0004-6361:20054590
- Althaus, L. G., Córscico, A. H., Isern, J., & García-Berro, E. 2010, A&A Rv, 18, 471, doi: 10.1007/s00159-010-0033-1

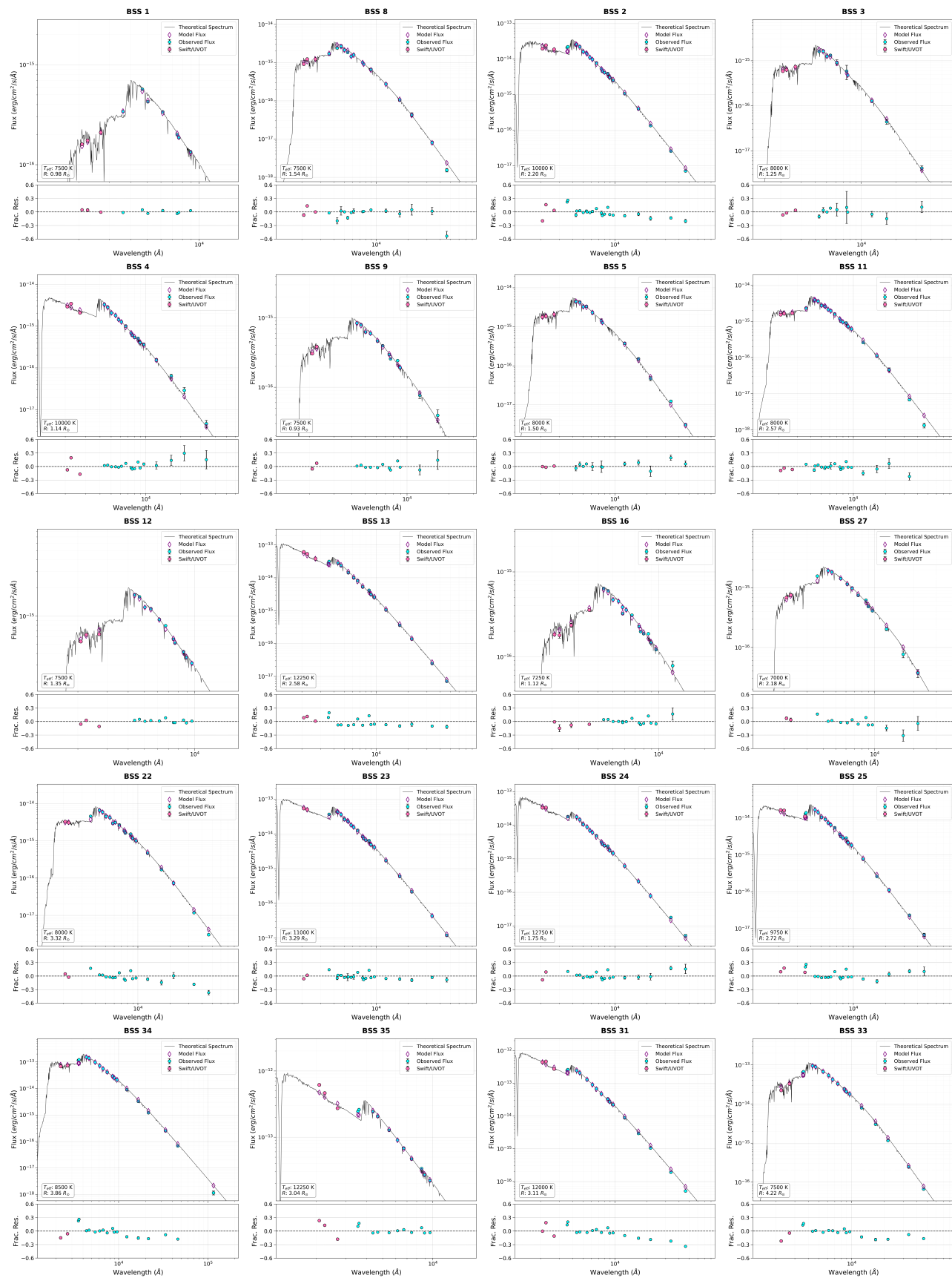


Figure 11. SED fits for the selected BSS stars.

**Table 9.** Fundamental properties of literature-studied hot component stars. Coordinates are given in degrees,  $T_{\text{eff}}$  in Kelvin, and luminosity, radius, and mass ( $L$ ,  $R$ ,  $M$ ) in solar units. The ‘‘Classification’’ column denotes stellar type, where BSS stands for ‘‘Blue Straggler Star’’ and BL stands for ‘‘Blue Lurker’’.

ID	Classification	Cluster	<i>Gaia</i> DR3 Source ID	$\alpha$ (deg)	$\delta$ (deg)	$T_{\text{eff}}$ (K)	$L$ ( $L_{\odot}$ )	$R$ ( $R_{\odot}$ )	$M$ ( $M_{\odot}$ )	Ref.
01	BSS	Berkeley 39	3056678372883126528	116.7569	-4.7046	12500	0.06	0.05	0.186* $\pm$ 0.092	01
02	BSS	King 2	424416887106018688	12.7354	58.1857	22000	3.10	0.12	0.222 $\pm$ 0.024	02
03	BSS	King 2	424415606039931520	12.8517	58.1522	24000	16.40	0.23	0.219 $\pm$ 0.055	02
04	BSS	King 2	424418398934484480	12.7482	58.2077	24000	2.70	0.10	0.214 $\pm$ 0.030	02
05	BSS	King 2	424418364574755328	12.7418	58.1967	26000	3.30	0.09	0.256 $\pm$ 0.029	02
06	BSS	King 2	424416234271059072	12.6768	58.1142	14000	1.90	0.23	0.206 $\pm$ 0.072	02
07	BSS	King 2	425074017100947968	12.4975	58.1352	19000	8.60	0.27	0.213 $\pm$ 0.029	02
08	BSS	M67	604917560635575808	132.8465	11.8028	11000	0.05	0.06	0.282 $\pm$ 0.057	03
09	BSS	Melotte 66	5507234395259864448	111.5865	-47.6962	38000	2.99	0.04	0.378 $\pm$ 0.102	04
11	BSS	NGC 2243	2893942062036322688	97.4233	-31.2615	19000	0.55	0.07	0.186* $\pm$ 0.023	05
12	BSS	NGC 2420	865405334273841536	114.7737	21.6450	11500	0.23	0.12	0.171 $\pm$ 0.051	06
13	BSS	NGC 2420	865401520342930560	114.6090	21.5778	10250	1.61	0.40	0.186* $\pm$ 0.008	06
14	BSS	NGC 2506	3038042784664224000	120.1130	-10.7665	19000	0.24	0.05	0.265 $\pm$ 0.022	07
15	BSS	NGC 2506	3038046358077125248	119.9990	-10.7541	15000	0.45	0.10	0.186* $\pm$ 0.037	07
16	BSS	NGC 2506	3038044880608396672	119.9921	-10.7650	13250	0.44	0.13	0.186* $\pm$ 0.021	07
17	BSS	NGC 2627	5504787948259881344	129.2610	-29.8309	14500	0.26	0.08	0.216 $\pm$ 0.033	08
25	BSS	NGC 7142	2217943209267285248	326.3131	65.8230	19750	0.10	0.03	0.319 $\pm$ 0.028	09
26	BSS	NGC 7142	2217989766712690432	325.9511	65.8598	15000	0.08	0.04	0.213 $\pm$ 0.003	09
27	BSS	NGC 7142	2218036534571068288	326.3476	65.8043	14000	0.09	0.05	0.202 $\pm$ 0.080	09
27	BSS	NGC 7142	2218036534571068288	326.3476	65.8043	14000	0.09	0.05	0.202 $\pm$ 0.080	09
28	BL	NGC 752	342917133876421760	29.2828	37.8243	14250	1.30	0.19	0.202 $\pm$ 0.020	10
29	BL	NGC 752	342918645704887040	29.4973	37.9149	13750	38.70	1.10	0.285 $\pm$ 0.024	10
30	BL	NGC 752	342864597836478080	29.5476	37.6592	10750	120.30	3.17	0.265 $\pm$ 0.023	10
31	BL	NGC 752	342893803614055168	29.6243	37.8603	9500	18.40	1.59	0.242 $\pm$ 0.045	10
32	BL	NGC 752	342921738081340928	29.2633	37.9290	14250	8.70	0.48	0.228 $\pm$ 0.006	10
33	BL	NGC 752	342914556896034176	29.2211	37.8692	15250	20.80	0.65	0.228 $\pm$ 0.006	10
34	BL	NGC 752	342915411593428736	29.1635	37.8614	15250	41.50	0.92	0.305 $\pm$ 0.092	10
35	BL	NGC 752	342866144024819840	29.6538	37.7529	13750	95.00	1.72	0.233 $\pm$ 0.032	10
36	BL	NGC 752	342917610616684032	29.3364	37.8619	12500	55.30	1.59	0.287 $\pm$ 0.073	10
37	BL	NGC 752	342919058020364544	29.3827	37.8945	12500	18.30	0.91	0.219 $\pm$ 0.029	10
38	BL	NGC 752	342869236401143808	29.4123	37.7700	12750	1.10	0.22	0.222 $\pm$ 0.020	10
39	BL	NGC 752	342918233388035328	29.4144	37.8737	11250	234.00	4.04	0.265 $\pm$ 0.006	10
40	BL	NGC 752	342870640854339200	29.4908	37.8061	11500	36.90	1.53	0.265 $\pm$ 0.015	10
41	BL	NGC 752	342864666555954048	29.5321	37.6658	11750	124.40	2.70	0.287 $\pm$ 0.026	10
42	BL	NGC 752	342920020094927104	29.4364	37.9884	15000	21.30	0.68	0.219 $\pm$ 0.005	10
43	BSS	NGC 7789	1995060313854772736	359.1755	56.7368	12500	1.29	0.24	0.202 $\pm$ 0.016	11
44	BSS	NGC 7789	1995020211733162112	359.5219	56.7841	15250	1.56	0.18	0.208 $\pm$ 0.004	11
45	BSS	NGC 7789	1995014237443527680	359.4574	56.7436	15000	0.26	0.08	0.219 $\pm$ 0.028	11
46	BSS	NGC 7789	1995010973268848512	359.4831	56.7121	15500	0.25	0.07	0.202 $\pm$ 0.072	11
47	BSS	NGC 7789	1995010801470149504	359.3789	56.6636	11750	0.67	0.20	0.222 $\pm$ 0.042	11

01: Chand et al. (2024a), 02: Jadhav et al. (2021), 03: Pandey et al. (2021), 04: Rao et al. (2022a), 05: Sheikh & Medhi (2024a), 06: Yadav et al. (2024), 07: Panthi et al. (2022), 08: Saketh et al. (2024), 09: Panthi et al. (2024), 10: Jadhav et al. (2024), 11: Vaidya et al. (2022b).

\*: Indicates that the mass value is adopted from the literature.

- Althaus, L. G., Miller Bertolami, M. M., & Córscico, A. H. 2013, *A&A*, 557, A19, doi: [10.1051/0004-6361/201321868](https://doi.org/10.1051/0004-6361/201321868)
- Angelo, M. S., Santos, J. F. C., & Corradi, W. J. B. 2020, *MNRAS*, 493, 3473, doi: [10.1093/mnras/staa517](https://doi.org/10.1093/mnras/staa517)
- Angelo, M. S., Santos, Jr., J. F. C., Maia, F. F. S., & Corradi, W. J. B. 2023, *MNRAS*, 522, 956, doi: [10.1093/mnras/stad1038](https://doi.org/10.1093/mnras/stad1038)
- Bailer-Jones, C. A. L., Rybizki, J., Fouesneau, M., Demleitner, M., & Andrae, R. 2021, *AJ*, 161, 147, doi: [10.3847/1538-3881/abd806](https://doi.org/10.3847/1538-3881/abd806)
- Bailyn, C. D. 1995, *ARA&A*, 33, 133, doi: [10.1146/annurev.aa.33.090195.001025](https://doi.org/10.1146/annurev.aa.33.090195.001025)
- Bayo, A., Rodrigo, C., Barrado Y Navascués, D., et al. 2008, *A&A*, 492, 277, doi: [10.1051/0004-6361:200810395](https://doi.org/10.1051/0004-6361:200810395)
- Bédard, A., Bergeron, P., Brassard, P., & Fontaine, G. 2020, *ApJ*, 901, 93, doi: [10.3847/1538-4357/abafbe](https://doi.org/10.3847/1538-4357/abafbe)
- Bilir, S., Taşdemir, S., Eraydın, E., et al. 2026, *Research in Astronomy and Astrophysics*, 26, 085002, doi: [10.1088/1674-4527/ae587d](https://doi.org/10.1088/1674-4527/ae587d)
- Binney, J., & Tremaine, S. 2008, *Galactic Dynamics: Second Edition*
- Bisht, D., Jiang, I.-G., Belwal, K., et al. 2026a, arXiv e-prints, arXiv:2604.12494, doi: [10.48550/arXiv.2604.12494](https://doi.org/10.48550/arXiv.2604.12494)
- Bisht, D., Jiang, I.-G., Elsanhoury, W. H., et al. 2026b, *AJ*, 171, 72, doi: [10.3847/1538-3881/ae285b](https://doi.org/10.3847/1538-3881/ae285b)
- Bovy, J. 2015, *The Astrophysical Journal Supplement Series*, 216, 29, doi: [10.1088/0067-0049/216/2/29](https://doi.org/10.1088/0067-0049/216/2/29)
- Bovy, J., & Tremaine, S. 2012, *The Astrophysical Journal*, 756, 89, doi: [10.1088/0004-637X/756/1/89](https://doi.org/10.1088/0004-637X/756/1/89)
- Breeveld, A. A., Landsman, W., Holland, S. T., et al. 2011, in *American Institute of Physics Conference Series*, Vol. 1358, *Gamma Ray Bursts 2010*, ed. J. E. McEnery, J. L. Racusin, & N. Gehrels (AIP), 373–376, doi: [10.1063/1.3621807](https://doi.org/10.1063/1.3621807)
- Bressan, A., Marigo, P., Girardi, L., et al. 2012, *MNRAS*, 427, 127, doi: [10.1111/j.1365-2966.2012.21948.x](https://doi.org/10.1111/j.1365-2966.2012.21948.x)
- Camisassa, M. 2025, *Astronomische Nachrichten*, 346, e20240118, doi: [10.1002/asna.20240118](https://doi.org/10.1002/asna.20240118)
- Carraro, G., Beletsky, Y., & Marconi, G. 2013, *MNRAS*, 428, 502, doi: [10.1093/mnras/sts038](https://doi.org/10.1093/mnras/sts038)
- Carraro, G., Geisler, D., Villanova, S., Frinchaboy, P. M., & Majewski, S. R. 2007, *A&A*, 476, 217, doi: [10.1051/0004-6361:20078113](https://doi.org/10.1051/0004-6361:20078113)
- Casamiquela, L., Blanco-Cuaresma, S., Carrera, R., et al. 2019, *MNRAS*, 490, 1821, doi: [10.1093/mnras/stz2595](https://doi.org/10.1093/mnras/stz2595)
- Castelli, F., Gratton, R. G., & Kurucz, R. L. 1997, *A&A*, 318, 841
- Castelli, F., & Kurucz, R. L. 2003, in *IAU Symposium*, Vol. 210, *Modelling of Stellar Atmospheres*, ed. N. Piskunov, W. W. Weiss, & D. F. Gray, A20
- Çınar, D. C., Tasdemir, S., Koc, S., & Iyer, S. 2024, *Physics and Astronomy Reports*, 2, 1, doi: [10.26650/PAR.2024.00002](https://doi.org/10.26650/PAR.2024.00002)
- Chand, K., Rao, K. K., Vaidya, K., & Panthi, A. 2024a, *AJ*, 168, 278, doi: [10.3847/1538-3881/ad85d2](https://doi.org/10.3847/1538-3881/ad85d2)
- . 2024b, *AJ*, 168, 278, doi: [10.3847/1538-3881/ad85d2](https://doi.org/10.3847/1538-3881/ad85d2)
- Chen, B., Stoughton, C., Yanny, B., et al. 2000, in *American Astronomical Society Meeting Abstracts*, Vol. 197, *American Astronomical Society Meeting Abstracts*, 13.08
- Chen, Y., Bressan, A., Girardi, L., et al. 2015, *MNRAS*, 452, 1068, doi: [10.1093/mnras/stv1281](https://doi.org/10.1093/mnras/stv1281)
- Childs, A. C., & Geller, A. M. 2025, *ApJ*, 989, 104, doi: [10.3847/1538-4357/ade9bc](https://doi.org/10.3847/1538-4357/ade9bc)
- Cutri, R. M., Wright, E. L., Conrow, T., et al. 2021, *VizieR Online Data Catalog: AllWISE Data Release (Cutri+2013)*, *VizieR On-line Data Catalog: II/328*. Originally published in: *IPAC/Caltech (2013)*
- Dattatreya, A. K., Yadav, R. K. S., Rani, S., et al. 2023, *ApJ*, 943, 130, doi: [10.3847/1538-4357/acad0](https://doi.org/10.3847/1538-4357/acad0)
- Dias, W. S., Monteiro, H., Moitinho, A., et al. 2021, *MNRAS*, 504, 356, doi: [10.1093/mnras/stab770](https://doi.org/10.1093/mnras/stab770)
- Donada, J., Anders, F., Jordi, C., et al. 2023, *A&A*, 675, A89, doi: [10.1051/0004-6361/202245219](https://doi.org/10.1051/0004-6361/202245219)
- Donor, J., Frinchaboy, P. M., Cunha, K., et al. 2020, *AJ*, 159, 199, doi: [10.3847/1538-3881/ab77bc](https://doi.org/10.3847/1538-3881/ab77bc)
- Eker, Z., Soyduğan, F., & Bilir, S. 2024, *Physics and Astronomy Reports*, 2, 41, doi: [10.26650/PAR.2024.00001](https://doi.org/10.26650/PAR.2024.00001)
- Eker, Z., Soyduğan, F., Soyduğan, E., et al. 2015, *AJ*, 149, 131, doi: [10.1088/0004-6256/149/4/131](https://doi.org/10.1088/0004-6256/149/4/131)
- Eker, Z., Bakış, V., Bilir, S., et al. 2018, *MNRAS*, 479, 5491, doi: [10.1093/mnras/sty1834](https://doi.org/10.1093/mnras/sty1834)
- El-Badry, K., Rix, H.-W., Quataert, E., Kupfer, T., & Shen, K. J. 2021, *MNRAS*, 508, 4106, doi: [10.1093/mnras/stab2583](https://doi.org/10.1093/mnras/stab2583)
- Ferraro, F. R., Beccari, G., Dalessandro, E., et al. 2009, *Nature*, 462, 1028, doi: [10.1038/nature08607](https://doi.org/10.1038/nature08607)
- Ferraro, F. R., Lanzoni, B., Dalessandro, E., et al. 2012, *Nature*, 492, 393, doi: [10.1038/nature11686](https://doi.org/10.1038/nature11686)
- Fitzpatrick, E. L. 1999, *PASP*, 111, 63, doi: [10.1086/316293](https://doi.org/10.1086/316293)
- Flewelling, H. A., Magnier, E. A., Chambers, K. C., et al. 2020, *ApJS*, 251, 7, doi: [10.3847/1538-4365/abb82d](https://doi.org/10.3847/1538-4365/abb82d)
- Fu, X., Bragaglia, A., Liu, C., et al. 2022, *A&A*, 668, A4, doi: [10.1051/0004-6361/202243590](https://doi.org/10.1051/0004-6361/202243590)
- Gaia Collaboration, Vallenari, A., Brown, A. G. A., et al. 2023, *A&A*, 674, A1, doi: [10.1051/0004-6361/202243940](https://doi.org/10.1051/0004-6361/202243940)

- Gehrels, N., Chincarini, G., Giommi, P., et al. 2004, *ApJ*, 611, 1005, doi: [10.1086/422091](https://doi.org/10.1086/422091)
- Geller, A. M., & Mathieu, R. D. 2011, *Nature*, 478, 356, doi: [10.1038/nature10512](https://doi.org/10.1038/nature10512)
- Gieles, M., Portegies Zwart, S. F., Baumgardt, H., et al. 2006, *MNRAS*, 371, 793, doi: [10.1111/j.1365-2966.2006.10711.x](https://doi.org/10.1111/j.1365-2966.2006.10711.x)
- Gosnell, N. M., Mathieu, R. D., Geller, A. M., et al. 2015, *ApJ*, 814, 163, doi: [10.1088/0004-637X/814/2/163](https://doi.org/10.1088/0004-637X/814/2/163)
- Hernquist, L. 1990, *ApJ*, 356, 359, doi: [10.1086/168845](https://doi.org/10.1086/168845)
- Hills, J. G., & Day, C. A. 1976, *Astrophys. Lett.*, 17, 87
- Hunt, E. L., & Reffert, S. 2024, *A&A*, 686, A42, doi: [10.1051/0004-6361/202348662](https://doi.org/10.1051/0004-6361/202348662)
- Indebetouw, R., Mathis, J. S., Babler, B. L., et al. 2005, *ApJ*, 619, 931, doi: [10.1086/426679](https://doi.org/10.1086/426679)
- Istrate, A. G., Marchant, P., Tauris, T. M., et al. 2016, *A&A*, 595, A35, doi: [10.1051/0004-6361/201628874](https://doi.org/10.1051/0004-6361/201628874)
- Jadhav, V. V., Pandey, S., Subramaniam, A., & Sagar, R. 2021, *Journal of Astrophysics and Astronomy*, 42, 89, doi: [10.1007/s12036-021-09746-y](https://doi.org/10.1007/s12036-021-09746-y)
- Jadhav, V. V., & Subramaniam, A. 2021, *MNRAS*, 507, 1699, doi: [10.1093/mnras/stab2264](https://doi.org/10.1093/mnras/stab2264)
- Jadhav, V. V., Subramaniam, A., & Sagar, R. 2023, *A&A*, 676, A47, doi: [10.1051/0004-6361/202345907](https://doi.org/10.1051/0004-6361/202345907)
- . 2024, *A&A*, 688, A152, doi: [10.1051/0004-6361/202450780](https://doi.org/10.1051/0004-6361/202450780)
- Jiménez-Esteban, F. M., Torres, S., Rebassa-Mansergas, A., et al. 2018, *MNRAS*, 480, 4505, doi: [10.1093/mnras/sty2120](https://doi.org/10.1093/mnras/sty2120)
- Karagöz, H., Yontan, T., Bilir, S., et al. 2025, *AJ*, 170, 149, doi: [10.3847/1538-3881/ade1f6](https://doi.org/10.3847/1538-3881/ade1f6)
- Keller, S. C., Schmidt, B. P., Bessell, M. S., et al. 2007, *PASA*, 24, 1, doi: [10.1071/AS07001](https://doi.org/10.1071/AS07001)
- Knigge, C., Leigh, N., & Sills, A. 2009, *Nature*, 457, 288, doi: [10.1038/nature07635](https://doi.org/10.1038/nature07635)
- Koester, D. 2010, *Mem. Soc. Astron. Italiana*, 81, 921, <https://arxiv.org/abs/1004.0348>
- Kruijssen, J. M. D. 2012, *MNRAS*, 426, 3008, doi: [10.1111/j.1365-2966.2012.21923.x](https://doi.org/10.1111/j.1365-2966.2012.21923.x)
- Lanzoni, B., Ferraro, F. R., Alessandrini, E., et al. 2016, *ApJL*, 833, L29, doi: [10.3847/2041-8213/833/2/L29](https://doi.org/10.3847/2041-8213/833/2/L29)
- Leigh, N., Sills, A., & Knigge, C. 2011, *MNRAS*, 415, 3771, doi: [10.1111/j.1365-2966.2011.18995.x](https://doi.org/10.1111/j.1365-2966.2011.18995.x)
- Leiner, E., Mathieu, R. D., Vanderburg, A., Gosnell, N. M., & Smith, J. C. 2019, *ApJ*, 881, 47, doi: [10.3847/1538-4357/ab2bf8](https://doi.org/10.3847/1538-4357/ab2bf8)
- Li, C., Zhong, J., Qin, S., & Chen, L. 2023, *A&A*, 672, A81, doi: [10.1051/0004-6361/202244998](https://doi.org/10.1051/0004-6361/202244998)
- Malhotra, S., Castro-Ginard, A., Anders, F., et al. 2026, *A&A*, 706, A62, doi: [10.1051/0004-6361/202557529](https://doi.org/10.1051/0004-6361/202557529)
- Marigo, P., Girardi, L., Bressan, A., et al. 2017, *ApJ*, 835, 77, doi: [10.3847/1538-4357/835/1/77](https://doi.org/10.3847/1538-4357/835/1/77)
- Mathieu, R. D., & Geller, A. M. 2009, *Nature*, 462, 1032, doi: [10.1038/nature08568](https://doi.org/10.1038/nature08568)
- Mathieu, R. D., & Geller, A. M. 2015, in *Astrophysics and Space Science Library*, Vol. 413, *Ecology of Blue Straggler Stars*, ed. H. M. J. Boffin, G. Carraro, & G. Beccari, 29, doi: [10.1007/978-3-662-44434-4\\_3](https://doi.org/10.1007/978-3-662-44434-4_3)
- Macted, P. F. L., Serenelli, A. M., Miglio, A., et al. 2013, *Nature*, 498, 463, doi: [10.1038/nature12192](https://doi.org/10.1038/nature12192)
- McCrea, W. H. 1964, *MNRAS*, 128, 147, doi: [10.1093/mnras/128.2.147](https://doi.org/10.1093/mnras/128.2.147)
- Mikhnevich, V. O., Plotnikova, A., Carraro, G., & Seleznev, A. F. 2026, *arXiv e-prints*, arXiv:2604.20722, doi: [10.48550/arXiv.2604.20722](https://doi.org/10.48550/arXiv.2604.20722)
- Milone, A. P., Piotto, G., Bedin, L. R., et al. 2012, *A&A*, 540, A16, doi: [10.1051/0004-6361/201016384](https://doi.org/10.1051/0004-6361/201016384)
- Minchev, I., Chiappini, C., & Martig, M. 2013, *A&A*, 558, A9, doi: [10.1051/0004-6361/201220189](https://doi.org/10.1051/0004-6361/201220189)
- Miyamoto, M., & Nagai, R. 1975, *Publications of the Astronomical Society of Japan*, 27, 533
- Nauenberg, M. 1972, *ApJ*, 175, 417, doi: [10.1086/151568](https://doi.org/10.1086/151568)
- Netopil, M., Oralhan, İ. A., Çakmak, H., Michel, R., & Karataş, Y. 2022, *MNRAS*, 509, 421, doi: [10.1093/mnras/stab2961](https://doi.org/10.1093/mnras/stab2961)
- Onken, C. A., Wolf, C., Bessell, M. S., et al. 2024, *PASA*, 41, e061, doi: [10.1017/pasa.2024.53](https://doi.org/10.1017/pasa.2024.53)
- Pandey, S., Subramaniam, A., & Jadhav, V. V. 2021, *MNRAS*, 507, 2373, doi: [10.1093/mnras/stab2308](https://doi.org/10.1093/mnras/stab2308)
- Panthi, A., & Vaidya, K. 2024, *MNRAS*, 527, 10335, doi: [10.1093/mnras/stad3887](https://doi.org/10.1093/mnras/stad3887)
- Panthi, A., Vaidya, K., Jadhav, V., et al. 2022, *MNRAS*, 516, 5318, doi: [10.1093/mnras/stac2421](https://doi.org/10.1093/mnras/stac2421)
- Panthi, A., Vaidya, K., Vernekar, N., et al. 2024, *MNRAS*, 527, 8325, doi: [10.1093/mnras/stad3750](https://doi.org/10.1093/mnras/stad3750)
- Patel, R. I., Metchev, S. A., & Heinze, A. 2014, *ApJS*, 212, 10, doi: [10.1088/0067-0049/212/1/10](https://doi.org/10.1088/0067-0049/212/1/10)
- Qin, S., Zhong, J., Anders, F., et al. 2026, *Research in Astronomy and Astrophysics*, 26, 015012, doi: [10.1088/1674-4527/ae1de1](https://doi.org/10.1088/1674-4527/ae1de1)
- Rain, M. J., Ahumada, J. A., & Carraro, G. 2021, *A&A*, 650, A67, doi: [10.1051/0004-6361/202040072](https://doi.org/10.1051/0004-6361/202040072)
- Rain, M. J., Pera, M. S., Perren, G. I., et al. 2024, *A&A*, 685, A33, doi: [10.1051/0004-6361/202347499](https://doi.org/10.1051/0004-6361/202347499)
- Randich, S., Gilmore, G., Magrini, L., et al. 2022, *A&A*, 666, A121, doi: [10.1051/0004-6361/202243141](https://doi.org/10.1051/0004-6361/202243141)
- Rani, S., Subramaniam, A., Pandey, S., et al. 2021, *Journal of Astrophysics and Astronomy*, 42, 47, doi: [10.1007/s12036-020-09683-2](https://doi.org/10.1007/s12036-020-09683-2)

- Rao, K. K., Vaidya, K., Agarwal, M., et al. 2022a, *MNRAS*, 516, 2444, doi: [10.1093/mnras/stac2241](https://doi.org/10.1093/mnras/stac2241)
- . 2022b, *MNRAS*, 516, 2444, doi: [10.1093/mnras/stac2319](https://doi.org/10.1093/mnras/stac2319)
- Rebassa-Mansergas, A., Solano, E., Jiménez-Esteban, F. M., et al. 2021, *MNRAS*, 506, 5201, doi: [10.1093/mnras/stab2039](https://doi.org/10.1093/mnras/stab2039)
- Roming, P. W., Townsley, L. K., Nousek, J. A., et al. 2000, in *Society of Photo-Optical Instrumentation Engineers (SPIE) Conference Series*, Vol. 4140, X-Ray and Gamma-Ray Instrumentation for Astronomy XI, ed. K. A. Flanagan & O. H. Siegmund, 76–86, doi: [10.1117/12.409161](https://doi.org/10.1117/12.409161)
- Roming, P. W. A., Kennedy, T. E., Mason, K. O., et al. 2005, *SSRv*, 120, 95, doi: [10.1007/s11214-005-5095-4](https://doi.org/10.1007/s11214-005-5095-4)
- Saketh, P., Panthi, A., & Vaidya, K. 2024, *AJ*, 168, 97, doi: [10.3847/1538-3881/ad5a96](https://doi.org/10.3847/1538-3881/ad5a96)
- Sandage, A. R. 1953, *AJ*, 58, 61, doi: [10.1086/106822](https://doi.org/10.1086/106822)
- Sheikh, A. H., & Medhi, B. J. 2024a, *AJ*, 168, 274, doi: [10.3847/1538-3881/ad84eb](https://doi.org/10.3847/1538-3881/ad84eb)
- . 2024b, *MNRAS*, 534, 4031, doi: [10.1093/mnras/stae2330](https://doi.org/10.1093/mnras/stae2330)
- Siegel, M. H., LaPorte, S. J., Porterfield, B. L., Hagen, L. M. Z., & Gronwall, C. A. 2019, *AJ*, 158, 35, doi: [10.3847/1538-3881/ab21e1](https://doi.org/10.3847/1538-3881/ab21e1)
- Sindhu, N., Subramaniam, A., & Radha, C. A. 2018, *MNRAS*, 481, 226, doi: [10.1093/mnras/sty2283](https://doi.org/10.1093/mnras/sty2283)
- Sindhu, N., Subramaniam, A., Jadhav, V. V., et al. 2019a, *ApJ*, 882, 43, doi: [10.3847/1538-4357/ab31a8](https://doi.org/10.3847/1538-4357/ab31a8)
- . 2019b, *ApJ*, 882, 43, doi: [10.3847/1538-4357/ab31a8](https://doi.org/10.3847/1538-4357/ab31a8)
- Singh, K. P., Tandon, S. N., Agrawal, P. C., et al. 2014, in *Society of Photo-Optical Instrumentation Engineers (SPIE) Conference Series*, Vol. 9144, *Space Telescopes and Instrumentation 2014: Ultraviolet to Gamma Ray*, ed. T. Takahashi, J.-W. A. den Herder, & M. Bautz, 91441S, doi: [10.1117/12.2062667](https://doi.org/10.1117/12.2062667)
- Skrutskie, M. F., Cutri, R. M., Stiening, R., et al. 2006, *AJ*, 131, 1163, doi: [10.1086/498708](https://doi.org/10.1086/498708)
- Spitzer, L. 1987, *Dynamical evolution of globular clusters* (Princeton University Press)
- Subramaniam, A., Pandey, S., Jadhav, V. V., & Sahu, S. 2020, *Journal of Astrophysics and Astronomy*, 41, 45, doi: [10.1007/s12036-020-09668-1](https://doi.org/10.1007/s12036-020-09668-1)
- Subramaniam, A., Sindhu, N., Tandon, S. N., et al. 2016, *ApJL*, 833, L27, doi: [10.3847/2041-8213/833/2/L27](https://doi.org/10.3847/2041-8213/833/2/L27)
- Taşdemir, S., Çınar, D. C., Canbay, R., et al. 2025, *Physics and Astronomy Reports*, 3, 1, doi: [10.26650/PAR.2025.00003](https://doi.org/10.26650/PAR.2025.00003)
- Taşdemir, S., & Yontan, T. 2023, *Physics and Astronomy Reports*, 1, 1, doi: [10.26650/PAR.2023.00001](https://doi.org/10.26650/PAR.2023.00001)
- Tandon, S. N., Subrahmanyam, R., Sinha, K. S., et al. 2017, *The Astronomical Journal*, 154, 128, doi: [10.3847/1538-3881/aa8451](https://doi.org/10.3847/1538-3881/aa8451)
- Tanık Öztürk, B., Bilir, S., Yontan, T., et al. 2025, *AJ*, 170, 164, doi: [10.3847/1538-3881/ade0](https://doi.org/10.3847/1538-3881/ade0)
- Taşdemir, S., Elsanhoury, W. H., Çınar, D. C., Haroon, A., & Bilir, S. 2026, *Research in Astronomy and Astrophysics*, 26, 045016, doi: [10.1088/1674-4527/ae3d11](https://doi.org/10.1088/1674-4527/ae3d11)
- Vaidya, K., Panthi, A., Agarwal, M., et al. 2022a, in 44th COSPAR Scientific Assembly. Held 16-24 July, Vol. 44, 2216
- Vaidya, K., Panthi, A., Agarwal, M., et al. 2022b, *MNRAS*, 511, 2274, doi: [10.1093/mnras/stac207](https://doi.org/10.1093/mnras/stac207)
- Vaidya, K., Panthi, A., Jadhav, V., et al. 2024, *Bulletin de la Societe Royale des Sciences de Liege*, 93, 250, doi: [10.25518/0037-9565.11667](https://doi.org/10.25518/0037-9565.11667)
- Wright, E. L., Eisenhardt, P. R. M., Mainzer, A. K., et al. 2010, *AJ*, 140, 1868, doi: [10.1088/0004-6256/140/6/1868](https://doi.org/10.1088/0004-6256/140/6/1868)
- Yadav, R. K. S., Dattatrey, A. K., Rangwal, G., et al. 2024, *ApJ*, 961, 251, doi: [10.3847/1538-4357/ad13e8](https://doi.org/10.3847/1538-4357/ad13e8)
- Yontan, T., & Canbay, R. 2023, *Physics and Astronomy Reports*, 1, 65, doi: [10.26650/PAR.2023.00008](https://doi.org/10.26650/PAR.2023.00008)
- Yücel, G., Canbay, R., & Bakış, V. 2024, *Physics and Astronomy Reports*, 2, 18, doi: [10.26650/PAR.2024.00003](https://doi.org/10.26650/PAR.2024.00003)
- Zeng, D., Mei, Y., Chi, H., Deng, H., & Wang, F. 2025, *ApJS*, 280, 74, doi: [10.3847/1538-4365/ae0643](https://doi.org/10.3847/1538-4365/ae0643)